Needle Shape Visualization, Tracking and Steering Control for Permanent Prostate Brachytherapy Applications

by

Michael Waine

A thesis submitted in partial fulfillment of the requirements for the degree of

Master of Science

in

Biomedical Engineering

Department of Electrical and Computer Engineering
University of Alberta

Abstract

Prostate cancer is one of the most prevalent types of cancers in North American males, afflicting one in eight men over the course of their lifetime [1]. Fortunately, early-stage prostate cancer has a wide variety of treatment options. One such option, permanent prostate brachytherapy, has been proven to have excellent survival rates for low to intermediate risk patients. However, the procedure has a steep learning curve and requires a long training period for new surgeons. Brachytherapy surgeons are also mostly located in urban areas. These factors can significantly limit patient access to procedure.

This thesis presents techniques designed to aid surgeons performing permanent prostate brachytherapy. Through the use of 2D ultrasound, we present techniques for needle shape reconstruction, tracking, trajectory prediction, and steering with the goal of improving the quality of information presented to prostate brachytherapy surgeons and helping them to perform the procedure with greater accuracy, consistency, and efficiency.

Preface

A brief introduction to the scope and focus of this thesis is provided in Chapter 1. As well, Chapter 1 includes a general literature survey, exploring some of the past work that has been performed with respect to needle shape visualization, trajectory prediction and steering control using ultrasound guidance. Chapter 2 will provide an overview of each chapter's contents, detailing our proposed strategies to make use of computer vision and robotic assistance to aid surgeons performing permanent prostate brachytherapy (PPB).

In Chapter 3, an algorithm for visualizing 3D needle shapes using ultrasound images is described in detail. Portions of Chapter 1.1 and all of Chapter 3 has been published in "Michael Waine, Carlos Rossa, Ron Sloboda, Nawaid Usmani, and Mahdi Tavakoli, 3D Needle Shape Estimation in TRUS-Guided Prostate Brachytherapy Using 2D Ultrasound Images, Biomedical and Health Informatics, IEEE Journal of, 2015." Nawaid Usmani and Mahdi Tavakoli were supervisory authors and, along with Ron Slobda, assisted with concept development and manuscript editing. Carlos Rossa aided in concept development, experimental setup construction, manuscript composition and editing. I was responsible for developing the needle shape reconstruction algorithm, conducting the experiments, analyzing the collected data, composing the manuscript and implementing the necessary revisions.

In Chapter 4, an algorithm for tracking the needle tip and predicting the needle tip's trajectory during insertion is described. Portions of Chapter 1.1 and all of Chapter 4 have been published in "Michael Waine, Carlos Rossa, Ron Sloboda, Nawaid Usmani, Mahdi Tavakoli, Needle Tracking and Deflection Prediction for Robot-Assisted Needle Insertion using 2D Ultrasound Images,

Journal of Medical Robotics Research, vol. 1, no. 1, 2016. (World Scientific)". Nawaid Usmani and Mahdi Tavakoli were supervisory authors and, along with Ron Sloboda, assisted with concept development and manuscript editing. Carlos Rossa aided in concept development, experimental setup construction, manuscript composition and editing. I was responsible for the development of the needle tracking algorithm and the needle trajectory prediction method, conducting the experiments, analyzing the collected data, and composing the manuscript.

In Chapter 5, a 3D needle steering controller is discussed. Portions of Chapter 5 have been prepared for journal publication with help from co-authors Carlos Rossa, Ron Sloboda, Nawaid Usmani, and Mahdi Tavakoli. Nawaid Usmani, and Mahdi Tavakoli were supervisory authors and, along with Ron Sloboda, assisted with concept development and manuscript editing. Carlos Rossa aided in experimental setup construction, manuscript composition and editing. I was responsible for the derivation of the control laws, conducting the experiments, analyzing the collected data, and composing the manuscript.

Acknowledgements

First, I would like to thank my supervisors Dr. Tavakoli and Dr. Usmani for all of the guidance, advice and support they have offered during my Master's degree, both in and out of academia. I would also like to thank Dr. Sloboda and Dr. Rossa for all of the help and feedback they've provided throughout my program.

Thank you to Alberta Innovates - Technology Futures, the Natural Sciences and Engineering Research Council and the University of Alberta for providing me with research funding throughout my program.

Finally, a special thank you to my parents and Monica for encouraging me through my post-secondary career. I am extremely grateful for all of the love and support you have given me.

Contents

1 Introduction **1**

1.1 Literature Survey 3

1.1.1 Needle Segmentation using US Images 3

1.1.1.1 Using 3D US Images for Needle Segmentation . 4

1.1.1.2 Using 2D Sagittal US Images for Needle Segmentation 5

1.1.1.3 Using 2D Transverse US Images for Needle Segmentation 5

1.1.2 Needle Modeling and Steering 6

1.1.2.1 2D Needle Steering Robots 7

1.1.2.2 3D Needle Steering Robots 7

2 Overview of Proposed Research **9**

2.1 Needle Shape Visualization 9

2.2 Needle Trajectory Prediction 10

2.3 Needle Steering 10

3 3D Needle Shape Visualization **12**

3.1 Problem Formulation 12

3.2 Locating Needle Point Candidates 14

3.2.1 Definition of the Region of Interest (ROI) 15

3.2.2 Contrast Enhancement 17

3.2.3 Candidate Needle Point Identification 18
3.3 Needle Shape Estimation using RANSAC 19
3.3.1 Fitting the Needle Point Candidates using RANSAC . . 20
3.3.2 Optimize Results 23
3.4 Experimental Setup Design 25
3.5 Results and Discussion 27
3.5.1 Effects of Image Depth on Needle Shape Estimation . . . 27
3.5.2 Effects of Image Quality on Needle Shape Estimation . . 30
3.6 Applications to Prostate Brachytherapy 32
3.6.1 Clinical Setup 32
3.6.2 Projection of 3D Needle Shape onto Sagittal Image Plane 34
3.6.3 Needle Shape Comparison Results and Discussion 36
3.7 Concluding Remarks 39

4 Needle Tracking and Trajectory Prediction 41
4.1 Problem Formulation 42
4.2 Real-time Needle Tracking in US Images 43
4.2.1 Image Processing 43
4.2.2 Kalman Filtering 45
4.3 Needle Modelling and Needle Tip Deflection Prediction 48
4.4 Experimental Setup 52
4.5 Experimental Results 54
4.5.1 Prediction of Needle Deflection 55
4.5.2 Online Needle Tip Prediction and Steering 55
4.6 Discussion 59
4.7 Concluding Remarks 61

5 Needle Steering 62
5.1 Problem Formulation 62
5.2 Integrator-Backstepping Controller 64

5.2.1 Needle Steering Control Using Integrator-Backstepping . 65
5.2.2 Vertical Deflection Control (VDC) 67
5.2.3 Horizontal Deflection Control (HDC) 69
5.2.4 Control Logic 71
5.3 Experimental Setup 72
5.3.1 Needle Steering Device 73
5.3.2 US Tracking 74
5.3.3 Tissue Phantom 74
5.4 Results 75
5.4.1 Simulation Results 75
5.4.2 Experimental Results 76
5.5 Discussion 81
5.6 Concluding Remarks 86

6 Conclusion **87**

6.1 Future Work 89

List of Tables

3.1 Patient Sample Statistics 33
3.2 Summary Statistics of Manual Comparison Results 37
3.3 Summary Statistics of Sagittal Image Comparison Results . . . 38

5.1 Comparison of Deflection Results in millimeters 78
5.2 Summary of Paired Sample t-Test Statistics 80

List of Figures

1.1 Illustration of permanent prostate brachytherapy 2

1.2 Example showing the difference between sagittal and transverse US imaging 4

3.1 An example of the needle appearance in a 2D transverse US image obtained during PPB 15

3.2 An example of a typical PPB setup 16

3.3 Image processing comparison 18

3.4 Flowchart summary of image processing procedure 19

3.5 Needle point candidate error definition 22

3.6 Example of 3D needle shape estimation using the proposed method 25

3.7 Experimental setup design 26

3.8 Contour plots showing final results 29

3.9 Samples of ROI's demonstrating four major issues affecting needle identification 30

3.10 Effects of confounding slices 32

3.11 Demonstration of the sagittal image plane angle estimated from a transverse US image 35

3.12 Comparison of the needle shapes obtained using the transverse and sagittal US images 37

4.1 An ultrasound image of the needle embedded within biological tissue 43

4.2 Needle shape modeling based on point loads applied to a cantilever beam 49
4.3 Needle insertion setup 52
4.4 Block diagram showing how the US probe is controlled through phases 1 and 2 54
4.5 Comparison of the predicted needle tip deflection error 56
4.6 Comparison of needle tip deflection for cases with rotation . . . 57
4.7 Comparison of the final tip deflection 58
4.8 Comparison of the prediction error 58

5.1 Bevel-tipped needle forces 63
5.2 Discontinuity logic flowchart 72
5.3 Needle steering device 73
5.4 Simulation results 77
5.5 Needle tip deflection comparison 79
5.6 Boxplot comparison results 80
5.7 Switching method example 81
5.8 Proposed 3D steering method example 82

List of Abbreviations

List of commonly used abbreviations

BPFS	Biochemical Progression-Free Survival
DOF	Degree of Freedom
IB	Integrator-Backstepping
PPB	Permanent Prostate Brachytherapy
RANSAC	Random Sample Consensus
ROI	Region of Interest
TRUS	Transrectal Ultrasound
US	Ultrasound

Chapter 1

Introduction

Prostate cancer is one of the most prevalent forms of cancer in Canadian men, with 1 in 8 males expected to develop prostate cancer at some point during their lifetime [1]. However, advances in screening and treatment have greatly reduced the mortality rate of prostate cancer, with only 1 in 28 males expected to die from the disease [1]. One treatment for early-stage prostate cancer that has seen a lot of recent success is permanent prostate brachytherapy (PPB).

PPB is a form of minimally invasive radiation therapy developed in the 1980's that involves applying a low dose of radiation to the prostate gland [2]. This is performed through the use of long, hollow, bevel-tipped needles that are filled with properly-spaced radioactive seeds. Surgeons insert these needles through the patient's perineum directly into the prostate. There, the seeds are ejected from the needle and permanently implanted within the prostate gland, where they apply a localized dose of radiation to the surrounding area. An illustration of PPB is shown in Fig. 1.1.

When performed properly, PPB has been shown to have excellent success rates, with 12-year biochemical progression-free survival (BPFS) rates of greater than 97% for implants that covered $> 90\%$ of the target volume [3]. However, for less adequate implants, this number can drop to 92% for low-risk patients or 86% for intermediate-risk patients [3].

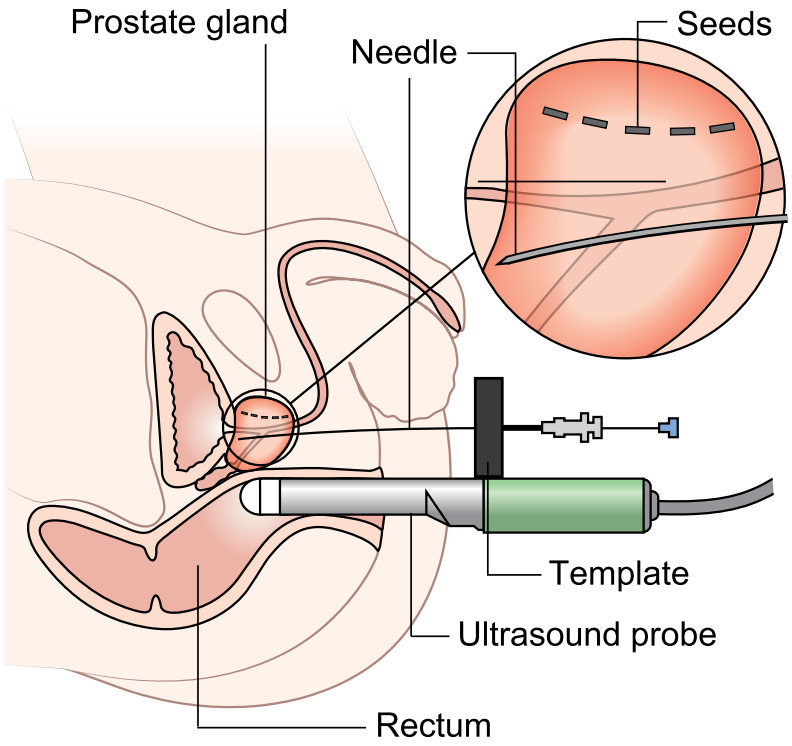

Figure 1.1: Brachytherapy needles filled with radioactive seeds are inserted through the perineum into the prostate. A template grid is used to help position the needles while a transrectal ultrasound probe is used to verify the results. *Image courtesy of Cancer Research UK / Wikimedia Commons*

Achieving a high-quality implant can be a difficult task for several reasons. First, brachytherapy needles are often 200 mm long, flexible, and bevel-tipped. These factors contribute to significant degrees of needle deflection during insertion into tissue. The needle's beveled tip generates an imbalance of forces applied to the needle's leading edge, which is the major cause of needle deflection during insertion. Second, tissue deformation can contribute to needle deflection and target motion. In PPB, the needle often traverses through multiple heterogeneous tissue layers, making it quite difficult to account for and predict how the needle will interact within the body. It takes a significant amount of experience and training for PPB surgeons to develop strategies to account for factors like needle deflection and tissue deformation, and organizations like the American Brachytherapy Society do not have well-defined needle

steering strategies that brachytherapy surgeons can follow [4]. This means that surgeons must rely on trial-and-error and personal experience to develop their own needle steering strategies.

One way to help reduce the training process and to help surgeons perform PPB with greater accuracy and consistency is to make use of advances in computer vision to improve the quality of feedback provided to surgeons and make use of robotics to assist surgeons during the needle insertion process.

1.1 Literature Survey

There are a variety of ways that advances in research and technology can be incorporated into PPB. Past work has explored ways to use US images to enhance information regarding the needle's shape and trajectory during the insertion process. As well, several research groups have researched ways to make use of needle steering robotics to help improve needle insertion procedures.

1.1.1 Needle Segmentation using US Images

Many groups have researched ways to automatically identify and track needles using ultrasound images. These methods can be divided into three main categories based on what type of US imaging is used: 3D volumetric, 2D sagittal, or 2D transverse images.

One form of 2D US images show the needle's longitudinal axis, as shown in Fig. 1.2a. These are referred to as sagittal images [5]. Sagittal images require the US transducer array to be positioned parallel to the needle's longitudinal axis. In contrast, images obtained perpendicular to the US transducer array, as in Fig. 1.2b, are known as transverse or axial US images. Some forms of transrectal US probes contain both sagittal and transverse transducers, like the example shown in Fig. 1.2.

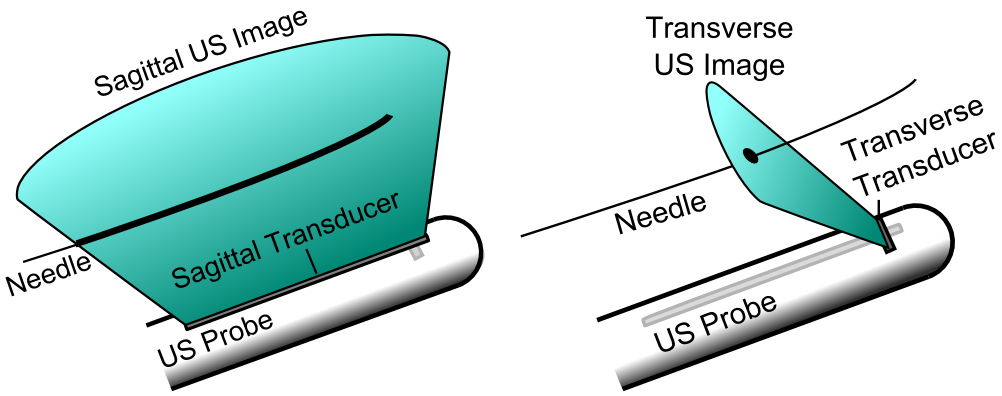

(a) Sagittal US Imaging (b) Transverse US Imaging

Figure 1.2: Example showing the difference between a) sagittal US imaging and b) transverse US imaging. Many clinical TRUS probes contain two transducer arrays to allow for both sagittal and transverse US imaging.

1.1.1.1 Using 3D US Images for Needle Segmentation

Various research studies have been performed on automatic object segmentation from 3D volumetric US images. Several methods have implemented the Radon and Hough transforms. For segmentation of surgical instruments, Novotny *et al.* [6] used a graphics processing unit operated in parallel architecture to perform their Radon transform-based method in real-time. Zhou *et al.* [7] and Qiu *et al.* [8] used a course-fine search strategy to allow for fast implementation of the 3D Hough transform for segmentation of straight needles [9]. Qiu *et al.* [10] also used phase-grouping combined with least-squares and 3D Hough transform optimization for real-time needle shape segmentation. Research on curved needle segmentation from 3D US includes a generalized Radon transform with Bezier curves [11], and the Hough transform combined with ray casting and polynomial approximation [12]. Alternatives to Radon/Hough transform-based methods include difference imaging techniques [13, 14] or RANSAC (random sample consensus)-based methods [15, 16, 17].

1.1.1.2 Using 2D Sagittal US Images for Needle Segmentation

Although some 3D US probes make use of 2D arrays to provide real-time 3D US, the majority of current clinical 3D US machines rely on sweeping a 1D array to produce a 3D volume. This technology is limited by slower frame rates and bulkier transducers compared to 2D US [18]. In addition, real-time 3D transrectal US (TRUS) probes are costly and are currently not widely available for use in clincal prostate brachytherapy. For this type of procedure, 2D US imaging methods are simpler to implement and allow for fast image processing capabilities.

Several research groups have used 2D sagittal imaging for needle segmentation, since a large portion of the needle can be visualized at once. Examples include work performed by Kaya *et al.* [19, 20], who combined Gabor filtering and RANSAC to estimate linear needle shapes, and work by Okazawa *et al.* [21], who used the Hough transform to estimate curved needle shapes. In addition, Ayvaci *et al.* [22] performed biopsy needle segmentation on TRUS videos for use in MRI/TRUS fusion guided biopsy. Work on needle tip tracking has been performed by Mathiassen *et al.* [23], who developed an optical tracking system based on intensity features in the images and Neubach *et al.* [24], who used a 30° needle-probe setup to improve visualization of the needle tip, and utilized image subtraction of subsequent frames for their needle steering robot.

1.1.1.3 Using 2D Transverse US Images for Needle Segmentation

Although sagittal US can be used to help visualize significant portions of the needle in a single image, in practice it is difficult to align the US transducer with the plane in which the needle deflects [25]. Additionally, alignment may not always be possible; for example, TRUS probes are limited to two degrees of freedom: translation parallel to the TRUS probe, and rotation about its sagittal axis. This limitation may prevent some needle shapes from being properly visualized, considering that the needle can deflect in any sagittal image plane,

or even multiple planes when rotation is introduced.

In prostate brachytherapy, instead of sagittal US imaging, transverse imaging is often used. Transverse US images provide surgeons with a consistent view of the prostate, regardless of where the needle was inserted, unlike sagittal imaging where the probe must be rotated after each insertion in order to locate the needle. As a result, transverse images are often used for pre-implant treatment planning and image registration during prostate brachytherapy [4]. Prostate brachytherapy equipment and software, such as the US stepper and the template grid previously shown in Fig. 1.1 are also designed for transverse imaging, making these type of images attractive for clincal use. However, in transverse images, only a cross-section of the needle is visible. Recent techniques have been developed by Greer *et al.* [26] and Adebar *et al.* [27], which integrate transverse US imaging with Doppler US for robotic needle steering. A voice coil actuator was attached to the needle to induce small vibrations that allow the needle to be seen in Doppler US. As well, Vrooijink *et al.* [28, 29] developed a method for real-time needle tip tracking using a motorized US probe. Another technique developed by Yan *et al.* [30] made use of difference imaging and shape-based level set segmentation for needle shape identification using transverse US images.

1.1.2 Needle Modeling and Steering

Needle modeling and steering within soft-tissue is a popular research topic [31]. Mechanics-based elastic beam models with virtual springs have been widely used for needle steering in [24, 32, 33, 34]. As well, a finite-element method with potential force-fields for needle steering and motion planning has been developed in [35, 36].

These type of models are often used to help inform needle steering robots. Most of these robots can be divided into two main groups: 2D steering robots vs. 3D steering robots.

1.1.2.1 2D Needle Steering Robots

There have been a variety of studies performed on 2D needle steering and the development of 2D needle steering robots. Most methods steer the needle through axial needle rotation, which adjusts the needle's bevel position such that the needle follows a desired curve or trajectory. For example, the needle steering robot developed by Neubach *et al.* [24] made use of a spring-based interaction model to inform their path planning algorithm. DiMiao and Salcudean [36] developed a system that made use of repulsion and attraction potentials to steer the needle and Abayazid *et al.* [34] developed both a kinematics and mechanics-based steering algorithm. Kallem and Cowan [37] developed a feedback linearization-based controller for out-of-plane deflection minimization, and Swensen *et al.* [38] improved on this design by incorporating torsional dynamics. Recently, Fallahi *et al.* [39] designed a non-model based, sliding controller, and Khadem *et al.* [40] developed a model-predictive controller for needle steering purposes. In these studies, the needle has either been assumed to remain in a single plane, or controlled to deflect within one plane without consideration of the needle's deflection within the other plane. However, factors such as tissue deformation can influence the needle's trajectory and lead to noticeable out-of-plane deflection. As well, deflection outside of a single plane is nearly inevitable unless the needle is completely stopped during the rotation process.

1.1.2.2 3D Needle Steering Robots

Some research groups have explored 3D needle steering strategies. Studies have been performed on laterally adjusting an external template or applying lateral forces at the needle base to affect the needle's trajectory during insertion, including [41, 42, 43, 44]. Other groups have focused on rotation-based 3D needle steering approaches, which typically allow for a more compact device. However, many performing research this area have focused on experiments utilizing very thin, nitinol wire as opposed to clinical needles, [27, 29, 45, 46,

47]. This can lead to the reliance of needle steering paths that are impossible in hospital settings due to the stiffness of clinical needles. Similarly, some groups have focused on the use of pre-bent or pre-curved needles [46, 47, 48], or needles containing internal concentric tubes to assist with needle steering [49, 50, 51, 52]. However, rotating these type of needles could potentially cause excessive tissue cutting and trauma. Additionally, in PPB, the interior of the needle is filled with the radioactive seeds, preventing other types of steering devices, such as actively controlled cannulas, to be inserted within.

Some groups such as [27, 29, 45, 53] make use of duty-cycling controllers, in which the needle is inserted with periods of no rotation or periods of continual rotation to control the degree of deflection at various stages of the insertion process [54]. Some duty-cycling controllers make use of rotation velocities of up to five rotations per second [29]. Yan *et al.* [55] have shown that the use of rotational drilling can be used to greatly reduce target movement and tissue deformation, but this type of "drilling" motion could have significant effects on tissue trauma, swelling, and recovery. This topic will be discussed in further detail in Chapter 5.

Chapter 2

Overview of Proposed Research

During PPB, hollow, flexible needles containing radioactive seeds are inserted into the prostate. The needle is monitored using ultrasound (US) imaging to verify placement accuracy. Once the needle is properly positioned, the seeds are permanently deposited within the prostate gland to apply a localized dose of radiation to the area. Therefore, the success of prostate brachytherapy critically depends on accurate placement of the seeds [59].

The goal of this thesis is to offer strategies to assist surgeons performing PPB. This is achieved through the use of techniques incorporating computer vision and/or surgical robotics. Ways to improve visual feedback during PPB surgery are discussed, with the intent of providing more useful, effective information to brachytherapy surgeons regarding the accuracy of the implants. As well, we discuss ways to use robotic assistance to aid with trajectory prediction and needle steering during the insertion process.

2.1 Needle Shape Visualization

In Chapter 3, we detail ways to visualize 3D needle shapes within tissue using 2D US images. The intent is to improve the visual feedback provided to PPB surgeons. Using 2D ultrasound, surgeons can use rudimentary methods

to verify needle insertion accuracy, such as comparing the needle tip location with the target location. However, this requires a significant amount of interpretation on the surgeon's part to determine precisely how the needle has deflected in 3D space. Chapter 3 demonstrates a method using random sample consensus (RANSAC) to help visualize precisely how the needle has deflected and deformed within tissue. Experiments are performed on transparent tissue phantoms in order to test the validity of this method. As well, the method is applied to clinical prostate brachytherapy US images to demonstrate the clinical relevance of the proposed approach.

2.2 Needle Trajectory Prediction

In Chapter 4, we present a method to automatically track the needle tip within 2D US images. This tracking method is incorporated into a kinematic, quasi-static needle-tissue interaction model to predict current and future needle tip deflection during the insertion process. Our idea is to prevent tissue compression and deformation caused by pressure applied by the US probe by limiting the movement of the probe itself. Using our proposed tip deflection prediction scheme, we can limit the depth into the body to which the probe must be inserted. Experiments are performed in *ex-vivo* biological beef tissue to demonstrate application of the proposed approach in robotic needle steering assistance.

2.3 Needle Steering

In Chapter 5, we detail a needle steering controller constructed using the nonlinear design tool known as Integrator-Backstepping. The controller is developed using a kinematic model of the needle motion during the insertion process. First, we demonstrate the design of two controllers, one which minimizes de-

flection on the horizontal plane, and one which minimizes deflection on the vertical plane. These controllers are then combined in tandem to develop a 3D needle steering control approach. The proposed method shifts between these two controllers based on the current needle deflection error along each plane. These controllers are tested through simulations as well as using multi-layered, heterogeneous *ex-vivo* biological tissue phantoms.

Chapter 3

3D Needle Shape Visualization

US imaging is widely used to guide percutaneous needle insertion procedures because of its accessibility, low-cost, non-ionizing nature, and real-time capability. These benefits come at the cost of image quality; US images provide low soft-tissue contrast resolution compared to modalities such as magnetic resonance imaging or computed tomography. In addition, US images often contain speckle artifacts, shadows, reverberations, and mirror image artifacts that require proper interpretation to fully understand. It is challenging for surgeons to perform complex tasks while accounting for these imaging limitations, or for US-guided robotic systems to distinguish US artifacts from intended targets. For these reasons, needle segmentation and shape estimation from US images is a challenging and important research topic.

3.1 Problem Formulation

In this chapter, we demonstrate a real-time needle segmentation algorithm based on 2D transverse images. As mentioned previously in Chapter 1, transverse imaging is commonly used for PPB applications, since they provide surgeons with a consistent view of specific prostate regions. The proposed method is most applicable for high dose-rate PPB applications, where radiation dosime-

try is adjusted in real-time based on needle insertion results. We implement strategies to handle the effects of needle rotation and use a-priori knowledge of the needle's initial position and orientation to reduce the number of images required for the proposed technique. As well, we test the algorithm on both *in-vitro* phantom tissue experiments and *in-vivo* prostate brachytherapy images. Our method does not require the use of specialized needle attachments unlike [26, 27, 28, 29], and can be readily incorporated with current clinical equipment. In contrast to [30], we used in-vivo prostate brachytherapy images and a threshold-based RANSAC approach to cope with the large amounts of noise and background objects present within clinical images. We also explored the number and depth at which the transverse images should be obtained for accurate needle shape estimations. Using a series of transverse US images, we apply image processing and a RANSAC algorithm to estimate the entire needle shape from the base of the needle to its tip. RANSAC has been successfully used for needle segmentation applications in 3D US images [15, 16, 17] and sagittal US images [19], but so far has not been applied to multiple transverse US images using *in-vivo* images.

By incorporating known spatial constraints on the needle along with a 3^{rd} order polynomial approximation, we can obtain reliable estimations of the entire needle shape for clinical applications. Third-order polynomials have been shown to provide a good approximation of surgical needle shapes [16, 21, 26, 27, 33] and prevent unrealistic rippling effects caused by higher-order polynomials. In addition, a low-order polynomial model is less computationally intensive for the RANSAC procedure compared to more complex, physics-based models. At the same time, our approach can cope with issues that complicate both manual and automated transverse US needle segmentation, such as cases where acoustic shadows camouflage the needle [12], or cases where the needle is difficult to distinguish from other nearby hyperechoic objects.

Insertion experiments are carried out on transparent tissue phantoms to

validate our proposed method and to determine the depth at which the images should be obtained as well as the overall image quality necessary to obtain accurate estimates. Analysis of clinical US images collected from human prostate brachytherapy procedures using the proposed method is also performed.

The rest of the chapter is organized as follows. Section 3.2 describes the process used to identify the needle within each transverse US image. In Section 3.3, the RANSAC algorithm used to estimate the 3D needle shape is described. Section 3.4 details the experimental setup and the phantom tissue experiments used to validate the accuracy of the proposed method. Experimental results are discussed in Section 3.5. In Section 3.6, applications with clinical data are demonstrated and discussed.

3.2 Locating Needle Point Candidates

During PPB, transverse US images of the needle embedded in tissue resemble Fig. 3.1. The needle appears as a hyperechoic object often followed by a comet-tail artifact, which is an artificial reverberation effect caused by the highly reflective needle surface [5]. Other hyperechoic objects may be visible in addition to the needle. For example, in Fig. 3.1, gel inserted into the urethra causes it to appear brighter than the needle itself, which allows the urethra to be used for landmarking purposes. The urethra travels directly through the prostate gland, making it a useful feature to identify during prostate brachytherapy. In addition, brachytherapy seeds and imaging noise can produce bright US intensities similar to the intensities caused by the needle. A study done by Wen *et al.* [60] showed that brachytherapy seeds could be segmented using similar techniques used in needle segmentation. Therefore, image processing must be performed to differentiate the needle from other hyperechoic objects or noise. Doing so involves defining a region of interest (ROI) and applying image enhancement techniques. It is assumed that all of the transverse US images used

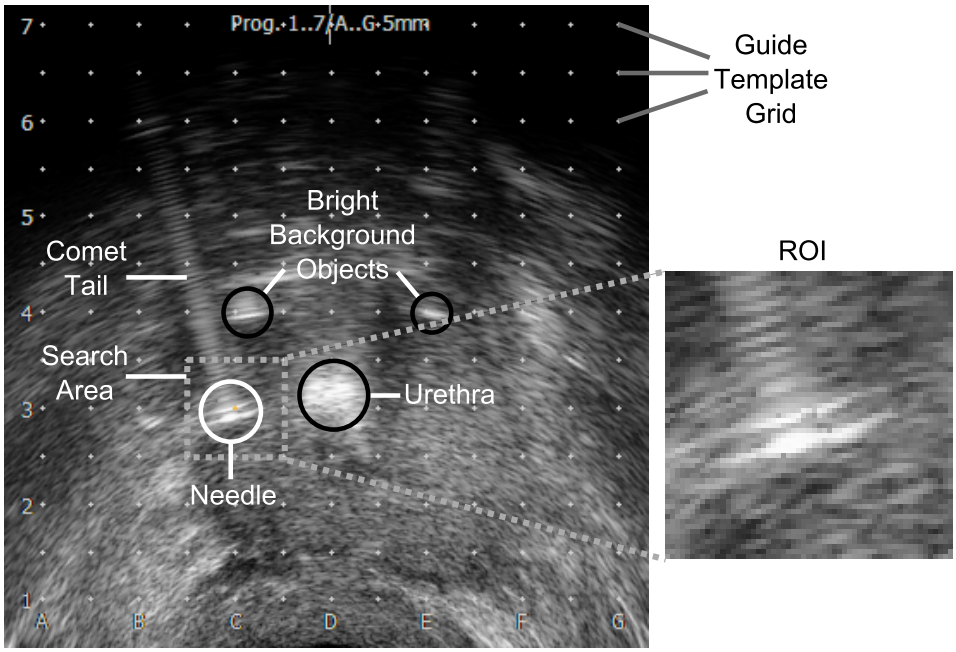

Figure 3.1: An example of the needle appearance in a 2D transverse US image obtained during PPB. The needle is circled in white and extraneous objects are circled in black. The ROI is shown on the right.

in the analysis were obtained along the needle, and correspond to either the needle shaft or the needle tip. This is confirmed by looking for a special double reflection feature that corresponds to the needle tip known as a "hamburger" signature before the transvere images are obtained from the US machine. As well, it is assumed that the depth of the needle within the tissue is also known. This is verified by recording the depth of the needle tip observed from the US machine before the transverse images are obtained.

3.2.1 Definition of the Region of Interest (ROI)

An example of a manual PPB setup is shown in Fig. 3.2. A template grid is used in the procedure to guide the needle towards the intended target [4]. An example showing the template grid superimposed on a transverse US image is shown in Fig. 3.1.

A dynamic region of interest (ROI) algorithm is used, based on methods

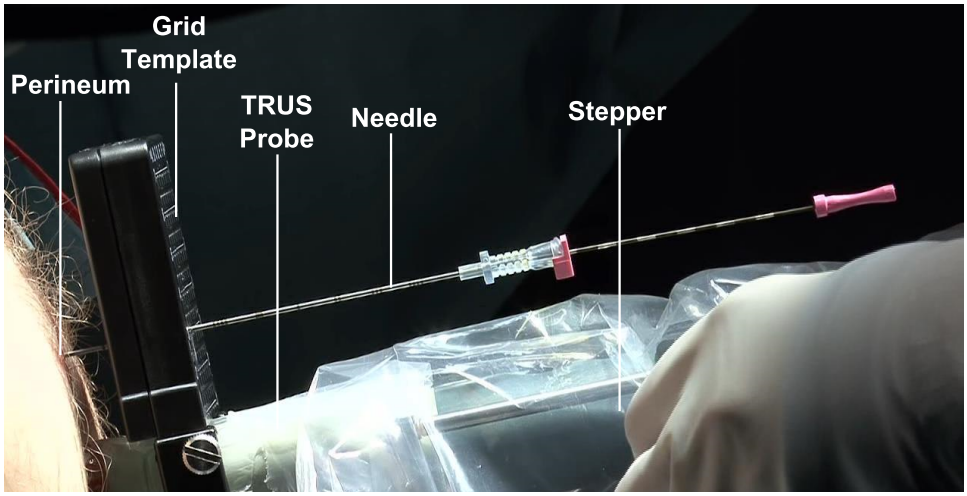

Figure 3.2: An example of a typical PPB setup. A stepper operated by the surgeon controls the depth of the US probe. A template grid is used to guide the needle towards the intended target during the procedure.

proposed in [24, 30]. First, a large ROI is selected in order to initially locate the needle, based on the template grid insertion location and the expected needle deflection at the initial depth of the transverse US images. This initial ROI for the in-vitro experiments was chosen as a 30 mm by 10 mm window and the ROI for the in-vivo patient study described in Section 3.6 was chosen as a 10 mm by 10 mm window. This variation was due to the a-priori knowledge of typical needle deflections observed for each case. The initial ROI for one of the clinical US images is shown and magnified in Fig. 3.1. This ROI is applied to the first three consecutive US images nearest to the needle base, and needle point candidates are identified within the images using the method described in Section 3.2.3. The needle location is then estimated using the method described in Section 3.3. If less than 30% of the expected needle point candidates are identified in the set of three images, the initial ROI is used again in the next set of three US images. Otherwise, the ROI is updated every three US images, which provides a fair trade-off between estimation accuracy and processing time. The updated ROI's are smaller than the originals (a 10 mm x 10 mm window for the in-vitro images and a 5 mm x 5 mm window for the

in-vivo images), which further reduces the amount of extraneous background objects located within the ROI. The updated ROI is centered around the needle location in the most recent image.

3.2.2 Contrast Enhancement

An intensity transformation $T(r)$ is applied to the ROI to improve contrast between the needle and the background. The transformation is

$$T(r) = r_{min} + (r_{max} - r_{min}) \left(\frac{r - r_{low}}{r_{high} - r_{low}} \right)^{\gamma} \tag{3.1}$$

where $r,\ r_{min},\ r_{max},\ r_{low},\ r_{high}$ represent normalized intensity values in the range $[0,\ 1]$. Here 0 represents the color black and 1 represents the color white. The values of r correspond to the pixel intensities contained in the original image. The range $[r_{min},\ r_{max}]$ defines the minimum and maximum desired intensities in the transformed image. The values r_{low} and r_{high} define saturation thresholds. Through equation (3.1), pixels in the ROI having intensities less than r_{low} are given the intensity r_{min} in the transformed ROI. Likewise, pixels with intensities larger than r_{high} are given the intensity r_{max}.

For our purposes, the desired spectrum is chosen to span $[0,\ 1]$ and the values r_{low} and r_{high} are set to 10% and 100% of the maximum intensity values present within the original ROI, respectively, causing a single-sided saturation of the (dark) background pixels. The value of γ specifies the shape of the exponential curve that maps the intensity values from the original ROI to the transformed ROI [61]. We set $\gamma > 1$ in order to apply additional weight towards lower intensity pixels, allowing for increased contrast between the needle and background. This combination of ROI and contrast enhancement yields consistent results, especially for the standard distances used in prostate brachytherapy (typically less than 50 mm between the needle and the US probe). Fig. 3.3 shows a comparison between the original ROI and the result after applying con-

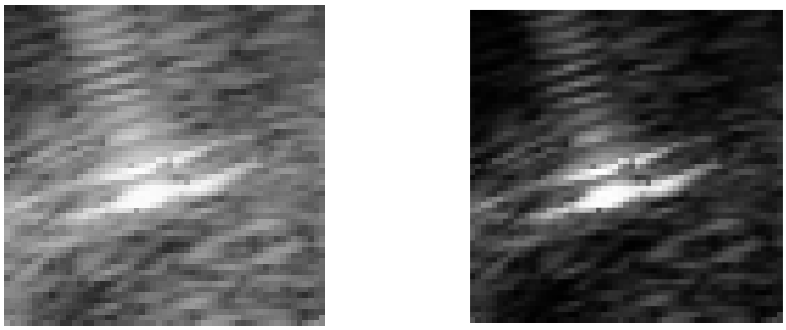

(a) Original Image (b) Intensity Transform

Figure 3.3: Comparison between a) the original image and b) the result after applying the intensity transform. Background noise is suppressed while the high contrast between the needle and background is retained.

trast enhancement. More recent filtering techniques used in the literature such as speckle reducing anistropic diffusion [62] or detail preserving anisotropic diffusion [63] were considered, but the advantages they provide are not applicable for our purposes of needle enhancement in transverse US images.

3.2.3 Candidate Needle Point Identification

After all image processing steps have been performed, a cumulative histogram of the pixel intensities in the ROI is obtained. The histogram is used to determine an intensity threshold α that corresponds to the n brightest pixels in the ROI, where n is defined by:

$$n = \frac{\beta A}{I_{dx} I_{dy}} \tag{3.2}$$

where A is the area of the needle cross-section in mm^2, I_{dx} and I_{dy} are the height and width in mm of a single pixel, and β is a tunable parameter to account for deterioration of the needle shape in the US image due to scattering and diffraction. In our work, we selected β to be 0.75 based on emperical results, meaning that 75% of the needle is expected to be visible in the US image. Pixels with intensities larger than α are considered as candidate needle points within the transverse US images and these candidate needle points are

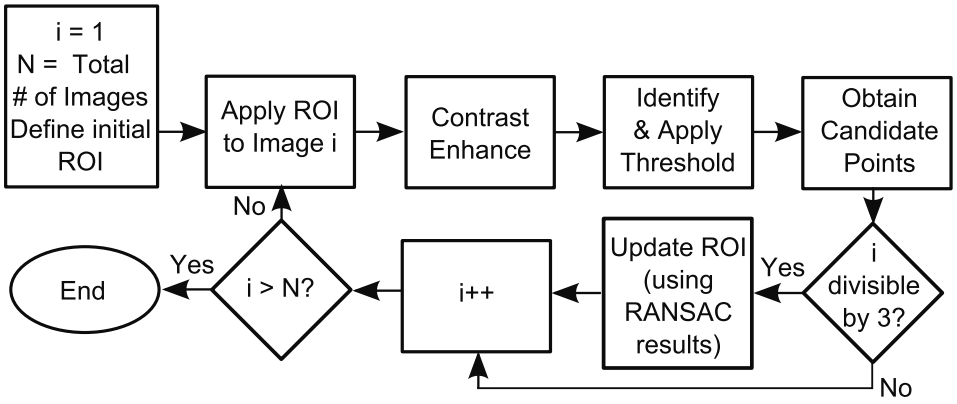

Figure 3.4: Flowchart summary of image processing procedure. For each transverse image, the ROI is applied, and image processing is used to locate needle point candidates. Every three images, RANSAC is applied to the needle point candidates and the results are used to update the ROI. The process continues until all images have been analyzed.

identified for each transverse image obtained along the needle. A flowchart showing the image processing steps is shown in Fig. 3.4.

Note that equation (3.2) provides a liberal estimate of the candidate needle points, since needle visibility is not yet taken into account. At this stage, it is difficult to determine which, if any, of the candidate needle points should be considered as outliers. A robust RANSAC-based method for detecting outliers based on the relative positions of the candidate needle points within each image along with the corresponding needle visibility in each image is described in the following section.

3.3 Needle Shape Estimation using RANSAC

There has been a variety of research performed in the area of needle steering during percutaneous needle insertion procedures [34, 64, 65]. Needle steering techniques exploit the fact that a needle with a bevelled tip follows a curved trajectory during insertion. Rotating the needle causes the position of the bevelled tip to change, which changes the needle's trajectory. Based on observation

of the steering techniques employed in our patient study, it is assumed that the needle rotates at most once during the insertion process. Therefore, we use a third-order polynomial to estimate the needle beginning from the template grid and ending at the needle tip.

The needle shape estimation algorithm used in this chapter is composed of two steps: 1) fit the needle point candidates using RANSAC, and 2) optimize the solution to the previous step via a weighted least squares regression.

3.3.1 Fitting the Needle Point Candidates using RANSAC

RANSAC is a robust model-fitting algorithm developed by Fischler and Bolles to smoothen data containing large amounts of gross outliers [66]. For example, in our case, calcifications, brachytherapy seeds, and microbubbles can produce false needle point candidates within the ROI defined in Section 3.2. If these objects are not intelligently removed, they can greatly influence the curve fit generated by a method such as Ordinary Least Squares Regression. The RANSAC Toolbox developed in [67] is used for implementation of the proposed algorithm.

We apply RANSAC multiple times so that the ROI described in 3.2.1 can be constantly updated. For every three US images, a new RANSAC procedure will be applied, and the needle point candidates identified from previous applications are carried forward.

The fundamental concept behind RANSAC involves iteratively sampling the minimum number of data points required for model estimation and comparing this estimation to the entire set of data points. A good model estimation corresponds to the model which fits the largest proportion of the data. Assume we have a model M with k solvable, free parameters. As well, assume we have a set S containing $N > k$ data points. A *random* selection of k points from S are sampled and used to solve for M. In our case, S refers to the combined set of needle point candidates identified in the transverse images analyzed so far, and M is the needle shape model. The needle shape model used for our work

is defined by the following equations:

$$x(d) = a_3 d^3 + a_2 d^2 + a_1 d + a_0 \tag{3.3}$$

$$y(d) = b_3 d^3 + b_2 d^2 + b_1 d + b_0 \tag{3.4}$$

$$z(d) = d \tag{3.5}$$

The value d represents the depth with respect to the grid template. The values (a_3, a_2, a_1, a_0) and (b_3, b_2, b_1, b_0) are the free parameters of the needle shape model. The (x, y, z) axes are defined in Fig. 3.5 with the coordinate frame origin at the intersection of the needle and the face of the grid template.

Because the needle is being inserted through the grid template, equations (3.3)-(3.5) can be simplified by incorporating the insertion location information into the model. In this work, the grid template is positioned to be exactly perpendicular to the US transducer and the calculated needle shape axes are aligned with the grid template. If the template is not perpendicular to the ultrasound transducer, a coordinate transformation matrix would be required to transform the image frames to the grid template frame before continuing with the procedure. This can be easily calculated if the position of the template with respect to the transducer is known. We assume the portion of the needle passing through the grid template holes is constrained to be approximately parallel to the z-axis. These constraints and the simplified model are summarized below:

$$x(0) = x_0,\ y(0) = y_0,\ \dot{x}(0) = 0,\ \dot{y}(0) = 0 \tag{3.6}$$

$$x(d) = a_3 d^3 + a_2 d^2 + x_0 \tag{3.7}$$

$$y(d) = b_3 d^3 + b_2 d^2 + y_0 \tag{3.8}$$

where $\dot{x}(d)$ and $\dot{y}(d)$ represent the first derivatives of equations (3.3)-(3.4). Equation (3.5) remains unchanged. In our case, equations (3.7)-(3.8) require

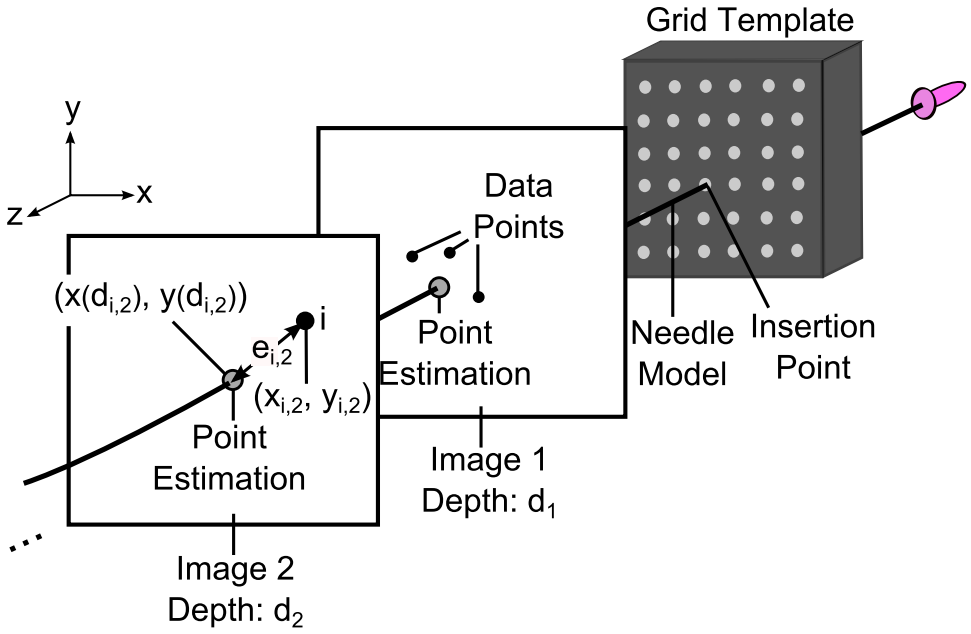

Figure 3.5: Diagram showing $e_{i,2}$ for the i^{th} point in the data set S.

$k = 2$ samples from S to solve for the free parameters. Let us refer to this parameterized model as M_1.

The values $(x_{i,j},\ y_{i,j},\ d_{i,j})$ identify the 3D coordinates of the i^{th} needle point candidate found within the j^{th} transverse image. The pair $(x_{i,j},\ y_{i,j})$ refers to point i's spatial coordinates within the j^{th} transverse image and $d_{i,j}$ refers to the depth of point i with respect to the grid template.

After solving for M_1, we identify the subset of points in S that adequately satisfies M_1. This subset is known as the consensus set CS_1 corresponding to M_1. CS_1 is determined from

$$CS_1 = \{(x_{i,j},\ y_{i,j},\ d_{i,j}) | e_{i,j}(d_{i,j}) < \tau\} \tag{3.9}$$

where

$$e_{i,j}(d_{i,j}) = \sqrt{(x_{p_2}(d_{i,j}) - x_{i,j})^2 + (y_{p_2}(d_{i,j}) - y_{i,j})^2} \tag{3.10}$$

The value τ specifies the inlier tolerance. We selected τ to be 0.635 mm, which is equal to the radius of an 18-gauge brachytherapy needle. The residual error

$e_{i,j}$ between the point i and the model M_1 is used to identify the needle points that satisfy the model. Next, a new iteration is performed, where the model is re-parameterized using a new random sample of k points to obtain M_2 and calculate the corresponding consensus set CS_2. This procedure is performed a minimum of N_c times, and a cost function is evaluated for each model and consensus set pair. The M-Estimator Sample Consensus (MSAC) technique developed by Torr *et al.* [68] is used to identify the model that minimizes the cost function

$$C = \sum_{j=1}^{N_I} \sum_{i=1}^{n_j} f(e_i), \;\; f(e_i) = \begin{cases} e_i, & e_i < \epsilon \\ \epsilon, & e_i \geq \epsilon \end{cases} \tag{3.11}$$

where N_I is the total number of transverse images analyzed so far, n_j is the number of needle point candidates in the j^{th} image, and ϵ is the cost function termination threshold. The consensus sets are ranked according to the inverse of their cost function magnitude. Once the change in the cost function for the highest ranked consensus set becomes smaller than ϵ, and at least N_c consensus sets have been obtained, the process terminates. At this point, a subset of the original needle point candidates has been identified; this subset excludes false positives. An initial curve fit describing the needle shape has also been identified. To summarize the RANSAC procedure thus far: two randomly-selected points from the data set are used to fit the needle shape model. Next, a consensus set is found, which includes needle point candidates that adequately satisfy the fitted model. Then, the quality of the model and corresponding consensus set is evaluated using MSAC. This is performed until a model with sufficient quality has been identified.

3.3.2 Optimize Results

The needle shape identified using the RANSAC procedure necessarily passes through at least two points as a result of Section 3.3.1. We optimize the curve fit by applying a weighted least squares regression to the consensus set

identified using the RANSAC algorithm. This is performed by minimizing the error estimates

$$s_x = \sum_{j=1}^{N_I} \sum_{i=1}^{n_{j,CS}} w_{i,j}(x_{p_2}(d_{i,j}) - x_{i,j})^2 \tag{3.12}$$

$$s_y = \sum_{j=1}^{N_I} \sum_{i=1}^{n_{j,CS}} w_{i,j}(y_{p_2}(d_{i,j}) - y_{i,j})^2 \tag{3.13}$$

$$w_{i,j} = \frac{(q-p)(r_{i,j} - r_{min,CS})}{r_{max,CS} - r_{min,CS}} + p \tag{3.14}$$

where $n_{j,CS}$ is the number of data points in the j^{th} transverse image of the consensus set, s_x and s_y are the error estimates with respect to x and y respectively, and $w_{i,j}$ is the weighting applied to the i^{th} data point of the j^{th} image. The value $r_{i,j}$ represents the intensity of the corresponding data point in the consensus set after the contrast enhancement steps described in Section 3.2.2 have been applied, $r_{min,CS}$ and $r_{max,CS}$ represents the minimum and maximum intensities within the consensus set respectively, and $[p, q]$ defines the desired range of the weighting values. Equations (3.12)-(3.14) give greater weighting to higher intensity pixels, which are more likely to correspond to the needle. For simplicity, the maximum intensity was given a weight of 1.0 and the minimum intensity was given a weight of 0.5. After the weighted least squares regression is applied to the data set, we obtain a 3D approximation of the needle shape starting from the template grid and ending at the most recent transverse image analyzed.

Note that the RANSAC procedure is applied multiple times in order to update the ROI between each application. In the first application of the RANSAC procedure, only the three transverse US images nearest to the needle base are analyzed, and inliers are obtained for each of these images. In the second application of RANSAC, the ROI is adjusted based on the most recent estimation of the needle location, and a new RANSAC procedure is applied to the next three transverse US images with the inliers from the previous application being

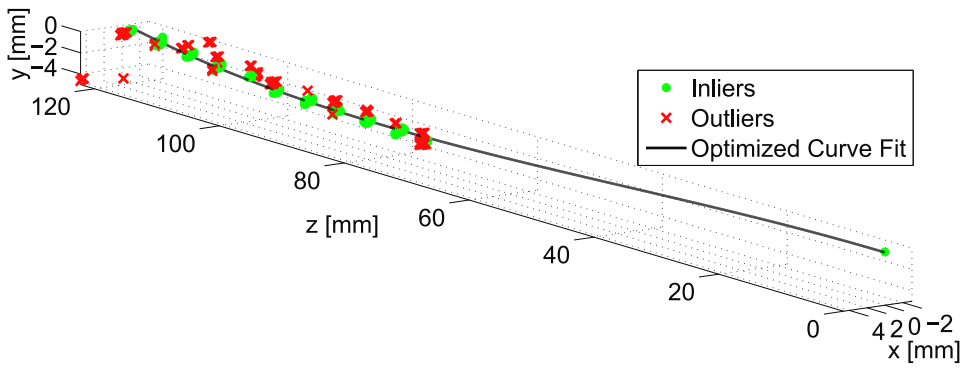

Figure 3.6: 3D needle shape estimation using the proposed method. The inliers represent the consensus set found using the RANSAC algorithm and the optimized curve fit is found through weighted least squares regression.

carried forward and the outliers being removed. This process repeats until all of the transverse US images have been analyzed.

The result is a 3D curve representing the needle shape beginning from the grid template and ending at the needle tip. An example is shown in Fig. 3.6, where the inliers and outliers represent true and false needle point candidates respectively, and the optimized curve fit is the needle shape obtained by incorporating equations (3.12)-(3.14).

3.4 Experimental Setup Design

The setup used to validate the proposed method is shown in Fig. 3.7a, and a sketch of setup mechanics is shown in Fig. 3.7b. An 18-gauge, bevel-tipped brachytherapy needle model PSS1820EZ (Worldwide Medical Technologies, Oxford, CT, USA) is manually inserted through a stabilizing template grid to a depth of 125 mm in a transparent tissue phantom created using a plastisol formula of two parts plastisol to one part plastic softener (M-F Manufacturing Company, Fort Worth, TX, USA). During insertion, the needle is manually rotated 90° at approximately half of the maximum insertion depth to simulate clinical practice and to generate needle deflection along multiple planes. A layer of US gel is applied to the top of the tissue phantom to ensure the

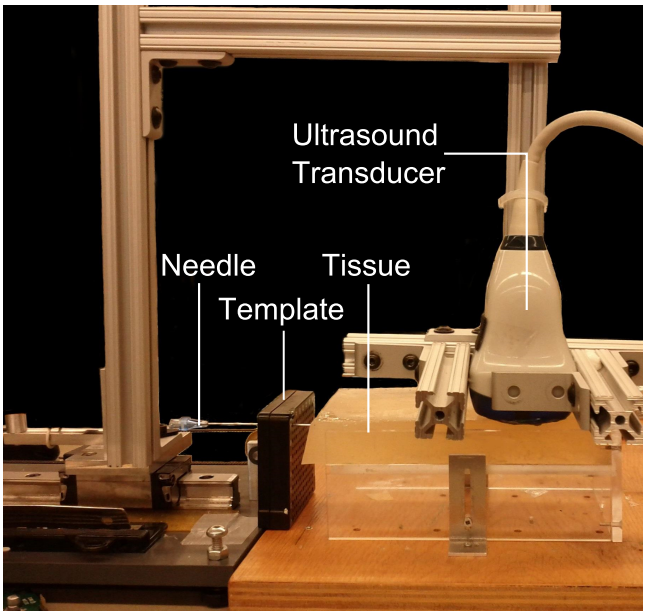

(a) Photograph of experimental setup

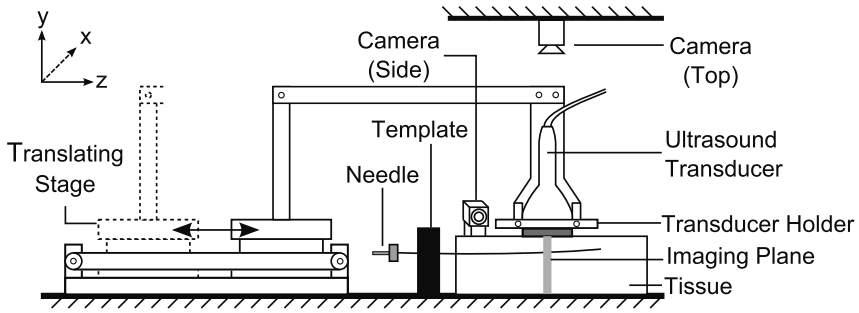

(b) Setup mechanics

Figure 3.7: a) The experimental setup and b) depiction of the setup mechanics. The US transducer is attached to a translating platform, which is manually adjusted to obtain axial slices of the embedded needle every 5 mm of depth.

US transducer probe makes appropriate contact with the tissue. A single-degree-of-freedom (DOF) translating platform is used to move the US probe. A mechanical holder is used to secure a linear US transducer model 4DL14-5/38 (Analogic Ultrasound, Richmond, BC, Canada) to the translating stage. The stage is manually positioned to allow for the collection of transverse US images of the needle every 5 mm along the z-axis, starting from a depth of 5 mm, mirroring clinical practice.

A total of 25 transverse images are collected along the needle length us-

ing a SonixTouch Ultrasound System (Analogic Ultrasound, Richmond, BC, Canada). As well, two XCD-SX90 cameras (Sony, Park Ridge, NJ, USA) are used to capture the true 3D needle shape. One camera is mounted above the setup to obtain a view of the $x-z$ plane and the second camera is mounted at the side to obtain a view of the $y-z$ plane.

Needle segmentation from the camera images is performed using MATLAB. Points corresponding to the needle are manually identified in the images obtained from the two cameras and a third-order polynomial in each of the $x-z$ and $y-z$ planes is used to obtain the 3D curve fit. This manually segmented needle shape is used for verification of the RANSAC algorithm results obtained from Section 3.3.

3.5 Results and Discussion

Two separate tests using the in-vitro US images obtained with the setup described in Section 3.4 are performed. The first test explores the optimal depths to obtain the transverse US images. The second test explores how the quality of the US images affected the needle shape estimation.

3.5.1 Effects of Image Depth on Needle Shape Estimation

The model described in Section 3.3 requires at least two different transverse images in order to characterize the needle shape. The 25 transverse images obtained from the experiment are grouped into subsets ranging from 2 successive slices to 25 successive slices, resulting in a total of 276 different image sets. For this stage of analysis, only successive slices were investigated in order to limit the number of image set combinations explored. The depth of the final slice is recorded for each image set, along with the "depth differential", which is found by subtracting the maximum transverse image depth from the minimum

transverse image depth. As well, for each image set, the residual error between the estimated needle shape obtained using the proposed method and the measured needle shape obtained using the camera images is calculated. This error is calculated every 0.01 mm along the needle and the average error is reported. Associated contour plots are shown in Fig. 3.8, where the maximum resultant error plot is shown in panel a) and the average resultant error plot is shown in panel b).

The contour plots show the needle shape error associated with each image set, where each image set is identified by its final slice depth, and its depth differential. The best results are those in dark blue, while poor results are those in dark red. The optimal combinations of depth differential and final slice depth for the maximum error contour plots are outlined in Fig. 3.8a. Needle shape errors of 2 mm or less are obtained when the final slice occurs at a depth of at least 95 mm, roughly 75% of the maximum insertion depth. Additionally, the depth differential has a significantly smaller effect on needle shape error than does the depth of the final slice. In general, as the depth of the final slice increases, the maximum needle shape error decreases, regardless of the depth differential. The exception occurs for very small depth differentials of less than 10 mm, which corresponds to image sets containing less than 3 images. There is likely not enough information contained in such small image sets to accurately characterize the needle shape.

The average error contour plot from Fig. 3.8b demonstrates that the overall needle shape estimation can be determined with an average error of 1 mm or less when the final slice occurs at a depth of at least 80 mm, regardless of depth differential. Again, the exception occurs for depth differentials of 10 mm or smaller. As well, the optimal results cover a larger area than those from Fig. 3.8a, demonstrating that the average needle shape error is quite robust with respect to the final slice depth.

The results demonstrate that the smallest errors are obtained with trans-

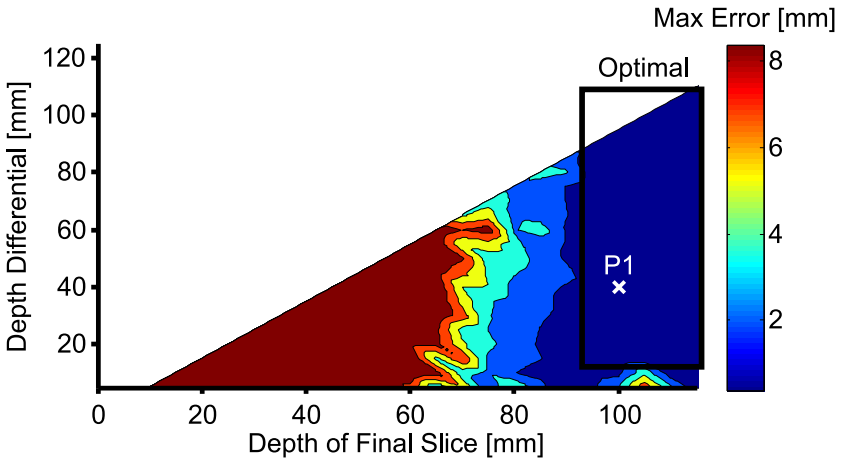

(a) Maximum resultant error

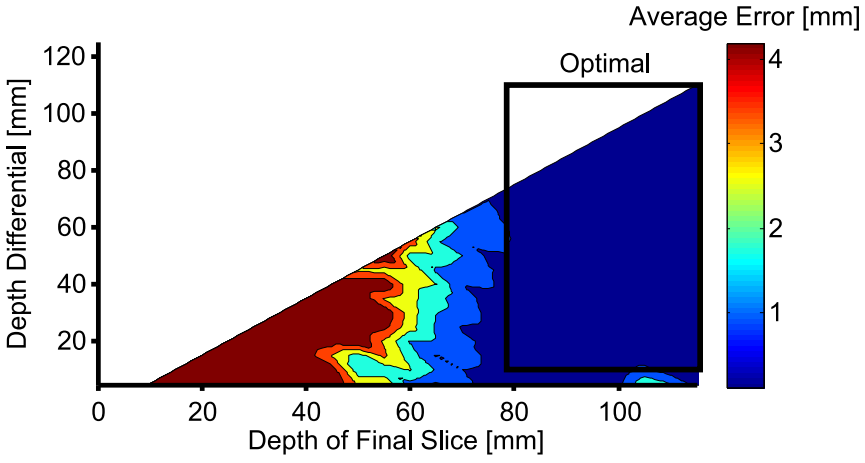

(b) Average resultant error

Figure 3.8: Contour plots showing the a) maximum error and b) average error obtained for each of the 276 transverse image sets. Example point P1 demonstrates the specific transverse image set whose final slice ends at 100 mm and contains a depth differential of 40 mm. Optimal combinations of depth differential and final slice depth are highlighted.

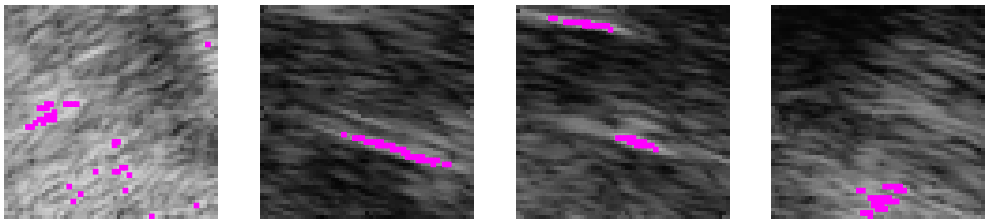

(a) Hidden (b) Distorted (c) Multiple (d) Unclear

Figure 3.9: Samples of ROI's demonstrating four major issues affecting needle identification. In a) the needle blends in with the surrounding tissue. In b) the needle can be seen, but its shape is distorted (elongated in this case). In c) there are two hyperechoic objects in the ROI. In d) a hyperechoic object is partially visible, but it is unclear whether it belongs to the needle.

verse image sets containing depth differentials of at least 10 mm, corresponding to 3 transverse slices, and where the final slice depth is at least 75% of the maximum depth.

3.5.2 Effects of Image Quality on Needle Shape Estimation

In clinical transverse US images, there are a variety of complications that affect identification of the needle. For example, in our patient study, of the 615 images obtained, the needle could be precisely identified through manual segmentation in 412 images, 67% of the total number. Of the remaining 33%, we found four major causes hindering needle identification: 1) the needle is not visible, 2) the needle image is distorted, 3) there are additional needle-like objects nearby, 4) a hyperechoic object is visible, but it does not have needle-like characteristics. An example of each case is shown in Fig. 3.9. Potential needle pixels identified using a simple thresholding algorithm are also highlighted in the figure, demonstrating how these issues adversely affect automated thresholding algorithms.

Transverse images where the needle cannot be clearly identified by traditional methods are denoted here as "confounding" images. A method was

developed to test the capabilities of our proposed algorithm to withstand the occurrence of these confounding images, specifically the type demonstrated in Fig. 3.9a where the needle cannot be identified at all. Based on the results of Section 3.5.1 along with the fact that the prostate typically spans 45-60 mm in length, we selected the final 10 images obtained during the experiment described in Section 3.4 to test the proposed algorithm. Confounding images were simulated by replacing one of the actual transverse US images with a blank image containing "false" needle point candidates placed randomly within the ROI. The image chosen to be replaced was randomized as well. The number of false needle point candidates to be inserted was selected as the average number of needle point candidates found in the remaining "true" images of the needle. Each false needle point candidate had the maximum intensity value in the grayscale range for simplicity. Simulations were performed to test the effects of 0 confounding images up to 9 confounding images. For each case, 100 simulations were performed and the effects on needle shape accuracy and simulation precision were recorded. A graph demonstrating the effects of confounding slices on needle shape accuracy is shown in Fig. 3.10a. The simulation precision represents the percentage of false needle point candidates included within the consensus set, and is shown in Fig. 3.10b.

Based on the results, the proposed algorithm can function sufficiently up to and including 7 confounding images, making it very robust to problems encountered in clinical US images. After this point, Fig. 3.10b shows that the precision degrades rapidly, which adversely affects the needle shape accuracy. Note that our proposed algorithm requires a minimum of 2 transverse images to operate properly. However, based on the results of Fig. 3.10, it appears that the use of 3 or more "relevant" transverse images obtained within 50 mm of the needle tip allows for more consistent needle shape estimations. Assuming that 33% of clinical transverse US images will have one of the issues demonstrated in Fig. 3.9, an average of 5 images would be necessary to obtain accurate results in

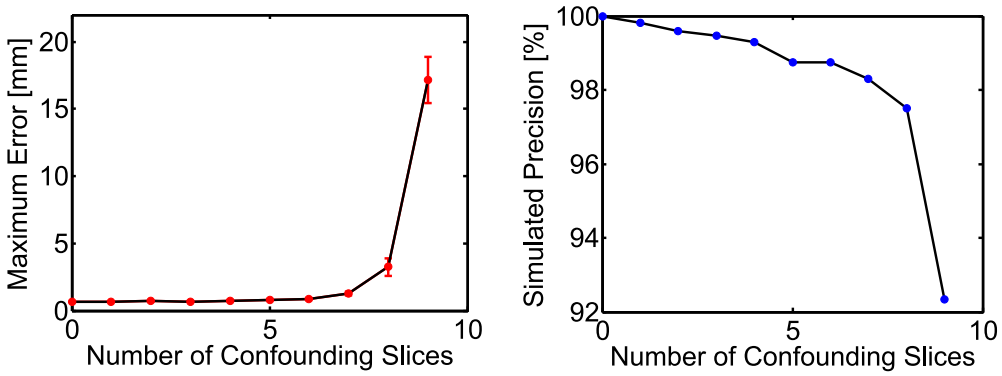

(a) Maximum Error (b) Precision

Figure 3.10: Effects of confounding slices on a) maximum error and b) precision. The number of confounding slices was varied from 0 to 9. In a), the mean and standard error obtained as a result of 100 simulations are plotted. In b) the precision over the course of 100 simulations is plotted.

clinical settings. This is a conservative estimate, since our proposed algorithm is robust against issues such as multiple or distorted needle-like objects that inhibit manual needle segmentation.

3.6 Applications to Prostate Brachytherapy

In this section, we discuss application of the proposed method to PPB.

3.6.1 Clinical Setup

A group of 17 patients undergoing PPB participated in our study[1]. Sample statistics of the patients are shown in Table 3.1. Transverse US images are obtained during the PPB procedures, which are used as inputs to the proposed method. For each patient, 1 to 4 needles are used for the study, yielding 49 needles in total. An experienced brachytherapy surgeon captured a set of 2D transverse US images for each inserted needle using a TRUS probe,

[1]Approval for this study granted by the Alberta Cancer Research ethics committee under file number 25837

Table 3.1: Patient Sample Statistics

Number of Patients	17	
Age	Median:	63
	Range:	51-69
Gleason Score	6:	12 (70.6%)
	7:	5 (29.4%)
Pretreatment PSA [ng/mL]	Median:	8.3
	Range:	3-12.9
Cancer Stage	T1c:	7 (41.1%)
	T2a:	8 (47.1%)
	T2b:	1 (5.9%)
	T2c:	1 (5.9%)
Risk Category	Low:	8 (47.1%)
	Intermediate:	9 (52.9%)

Type 8848 (BK Medical, Peabody, MA, USA). The images are captured at 5 mm intervals using a manually operated Civco Classic Stepper (Civco, Orange City, IA, USA). The images are spaced as such in order to match the template grid spacing, which is 5 mm both horizontally and vertically. This is a well-established clinical geometry used in prostate brachytherapy equipment and for seed placement planning. The images begin at the needle tip and span the entire prostate, resulting in a set of 10 to 13 images, depending on the length of the patient's prostate. In order to locate the needle tip, the surgeon monitored the US images near the prostate base and looked for a "hamburger" signature, a special double reflection artifact that is caused by the bevelled needle tip. A 2D sagittal US image is also obtained for each needle and is used to compare the results from the proposed method for verification. Each sagittal image captured a 50 mm to 60 mm needle segment which included the needle tip. The 3D needle shape was calculated using the steps outlined in Section V and its 2D projection in the sagittal image plane is compared to the sagittal US image obtained by the surgeon.

3.6.2 Projection of 3D Needle Shape onto Sagittal Image Plane

Before the 3D needle shape estimated using the proposed algorithm can be compared to the sagittal image obtained clinically, we must first project the needle shape estimate onto the sagittal image plane. Because the TRUS probe is cylindrical, all sagittal imaging planes pass directly through the center of the probe. The probe's cross-sectional radius is 9.3 mm, and so the center of the probe can be easily determined in the US image. Next, we estimate the angle of the sagittal image plane for each of the transverse US images, denoted as θ_j, where j refers to the index of the transverse image. An example for a single transverse US image is shown in Figure 12. θ_j can be calculated as

$$\theta_j = \begin{cases} \text{atan}\frac{y_n - y_c}{x_n - x_c}, & x_n > x_c \\ \pi + \text{atan}\frac{y_n - y_c}{x_n - x_c}, & x_n < x_c \\ \frac{\pi}{2}, & x_n = x_c \end{cases} \tag{3.15}$$

where $(x_n,\ y_n)$ represents the needle point estimation obtained using the method described in Section 3.2 and $(x_c,\ y_c)$ represents the center of the US probe. The estimated angle of the sagittal image plane will be the average of all θ_j values for the same needle.

The estimated sagittal imaging plane is calculated for each transverse image and the mean angle is obtained. The mean angle is used to derive the transformation matrix T_p which is used to convert the 3D needle points $(\vec{x}_{3D},\ \vec{y}_{3D},\ \vec{z}_{3D})$ to their 2D projection $(\vec{x}_{proj}, \vec{y}_{proj})$ onto the estimated sagittal plane. The transformation is shown below:

$$\begin{bmatrix} x_{proj,1} & \cdots & x_{proj,n} \\ y_{proj,1} & \cdots & y_{proj,n} \\ z_{proj,1} & \cdots & z_{proj,n} \\ 1 & \ldots & 1 \end{bmatrix} = T_{proj} \begin{bmatrix} x_{3D,1} & \cdots & x_{3D,n} \\ y_{3D,1} & \cdots & y_{3D,n} \\ z_{3D,1} & \cdots & z_{3D,n} \\ 1 & \ldots & 1 \end{bmatrix} \tag{3.16}$$

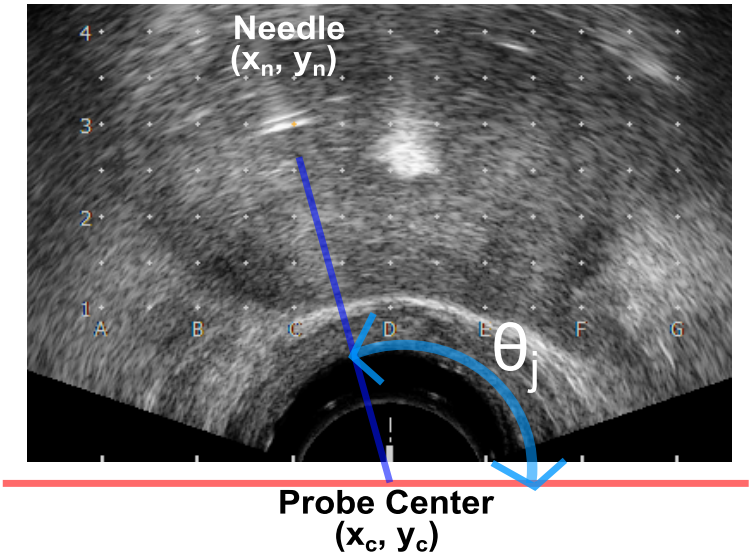

Figure 3.11: Demonstration of the sagittal image plane angle estimated from a transverse US image.

$$T_{proj} = \begin{bmatrix} 0 & 0 & 1 & 0 \\ \cos\theta & \sin\theta & 0 & 0 \\ -\sin\theta & \cos\theta & 0 & 0 \\ 0 & 0 & 0 & 1 \end{bmatrix} \tag{3.17}$$

Here n is the total number of points defining the 3D needle shape. We refer to this 2D projection as the projected needle shape. The needle shape obtained from the sagittal US image will be referred to as the sagittal needle shape.

The needle shape computations described in Sections 3.2 and 3.3 were applied to the clinical US images using a 2.6 GHz AMD Phenom II X4 910 processor with 4 GB of memory running 32 bit MATLAB. The mean computation times for the image processing (per image) and the needle shape estimation portions of the algorithm were 22 ms and 351 ms respectively. The needle shape estimation was calculated using the entire set of transverse images obtained for each needle studied and a minimum of 100 consensus set iterations. The computation times show that the needle shape estimation can be obtained and displayed in real-time for clinical applications and will not impact the overall

procedure time.

3.6.3 Needle Shape Comparison Results and Discussion

Needle point estimation results were compared to manual segmentation using the transverse US image sets obtained from the patient study. These images were selected based on how readily the needle could be manually identified within the image. The needle location was manually identified in each of the transverse US images and the result was compared to two separate applications of the proposed algorithm. In the first application, the entire transverse image set was used as an input to the proposed algorithm. In the second application, the 5 transverse images obtained nearest to the needle tip were used as inputs. The latter application demonstrates how the proposed method functions using a limited set of images, some of which may contain confounding information. Summary statistics are shown in Table 3.2. Using the entire image set, the resultant error between the manual segmentation results and the proposed method averages 0.4 mm, which equates to only 2 pixels in the transverse US image. With the image set of 5 transverse images, the resultant error averages 0.5 mm, which equates to 3 pixels in the transverse US image. In both cases, the needle shape estimation results obtained using the proposed algorithm averaged close to 0.5 mm of the manual needle segmentation results. Note that manual segmentation involves a degree of human subjectivity and imprecision, which accounts for the vast majority of the smaller errors shown in Table 3.2. Our method provides a consistent, systematic way to locate the needle based on the estimated needle position observed within a series of images.

The projected needle shape was also compared to the needle segment observed in the sagittal US image as a second way to validate the results. For each sagittal US image, the image processing algorithm described in Section 3.2 is applied, and the RANSAC algorithm described in Section III is slightly modified to fit a second-order polynomials to the needle segment. A second-order

Table 3.2: Summary Statistics of Manual Comparison Results

	Entire Transverse Image Set		
	Error: x-axis	Error: y-axis	Resultant Error
Mean [mm]	0.3	0.2	0.4
Std. Dev. [mm]	0.3	0.4	0.5
	5 Transverse Images		
	Error: x-axis	Error: y-axis	Resultant Error
Mean [mm]	0.4	0.3	0.5
Std. Dev. [mm]	0.5	0.6	0.8

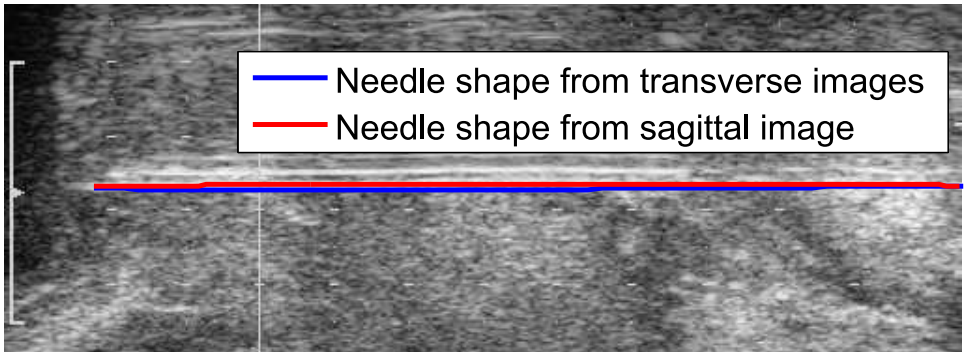

Figure 3.12: Comparison of the needle shapes obtained using the transverse and sagittal US images.

polynomial was used because the portion of the needle observed in the sagittal US images is approximately half the inserted length. The needle tip was localized in the sagittal images using a similar method to [16], where the needle tip is marked by a drop-off in pixel intensity below the intensity threshold α defined in Section 3.2.3. In addition, the 18 gauge brachytherapy needles used are not as flexible as alternatives used in the literature like nitinol wire. A second-order polynomial is sufficient to estimate this needle segment, as opposed to a third-order polynomial which is reserved for estimation of the entire needle shape.

The sagittal and projected needle shapes are aligned at the point closest to the needle base in the sagittal image. An example of the two needle shapes superimposed over the original image is shown in Fig. 3.12.

Table 3.3: Summary Statistics of Sagittal Image Comparison Results

	Entire Transverse Set		**5 Transverse Images**	
	Max Error	Avg. Error	Max Error	Avg. Error
Mean [mm]	0.70	0.37	0.91	0.43
Std. Dev. [mm]	0.32	0.15	0.67	0.21

The maximum error between the two needle shapes is measured along with the average error between the estimated needle shape (obtained from the transverse US images) and the reference needle shape (obtained from the sagittal US image). Summary statistics for all 49 needles are presented in Table 3.3.

Based on the results in Table 3.3, we observe that the maximum error between the two needle shapes averages 0.70 mm when using the entire transverse image set and 0.91 mm when using only 5 transverse images, both of which are less than the outer diameter of an 18 gauge brachytherapy needle (1.27 mm). The average errors of 0.37 mm for the entire transverse image set and 0.43 mm for the 5 transverse image set corresponds to an errors of 2.1 pixels and 2.4 pixels in the clinical transverse US images respectively, which is very minimal. An average accuracy of $<$0.5 mm is sufficient for clinical applications, where, based on our clinical study, surgeons can tolerate errors of up to 5 mm with respect to the needle's target position. These results indicate that the proposed method can provide accurate estimates of the needle shape under clinical conditions. This method allows clinicians to use transverse US images to develop an estimate of the 3D needle shape quickly without requiring 3D US or sagittal images. In addition, the quality of the needle shape information provided by the proposed method is much better than the information surgeons currently use to verify needle placement, which is typically the lateral error observed in a single tranverse US image. This type of technology could be very useful for high dose-rate PPB applications, where the radiation dosimetry is adjusted in real-time to adapt to the needle placements.

3.7 Concluding Remarks

In this chapter, a method for 3D needle shape visualization using a discrete series of transverse images is described. Experiments are performed to identify the depth, number, and quality of transverse images required to obtain accurate results. As well, application of the proposed method to patient data is performed and verified by comparing the estimation results to images obtained from the sagittal perspective and to manual segmentation of the transverse US images.

Experimental results showed that to obtain maximum errors of less than 2 mm, the depth of the final image within the transverse image set must be at least 75% of the maximum needle depth into tissue. Additional tests showed that using 10 transverse images closest to the needle tip, the proposed method is functional as long as the needle can be identified in 30% of the images obtained. Our method is robust against many of the common US characteristics that confuse both manual and automated segmentation methods.

The proposed method was also applied to *in-vivo* images obtained from prostate brachytherapy procedures. Two different tests were performed. In the first test, each needle shape was estimated using the entire set of *in-vivo* transverse US images obtained. In the second test, each needle shape was estimated using the 5 transverse US images obtained nearest to the needle tip. The results were compared to manual segmentation of the same images. The error between the manually segmented results and the results obtained using the proposed method was 0.4 mm when using the entire transverse US image sets and 0.5 mm when using the 5 transverse US image sets. The needle shape estimations for each case were also compared to sagittal images obtained during the brachytherapy procedure. Comparisons yielded a maximum error averaging 0.70 mm when using the entire transverse image sets and 0.91 mm when using the 5 transverse image sets. A study of computation times showed

that the result could be accurately obtained in real-time for operating room conditions.

With respect to the clinical US images, although the comparison could only be performed on the segment of the needle observed in the sagittal US plane, this segment normally spans the entire length of the prostate or slightly greater. Therefore, the proposed method is shown to provide excellent results for the needle shape observed within the prostate, which is normally the segment of greatest interest for determining the dose distribution. The average errors observed in the clinical US images were slightly higher than those obtained in the in-vitro experiments, which could be caused by larger degree of noise and hyperechoic objects found when imaging human tissue compared to the plastisol tissue phantom. Although the proposed method was demonstrated using data from low-dose rate PPB cases, it could readily applied to high-dose rate PPB and could potentially be of great use in this area, since real-time dose distribution calculations are prominently implemented.

Chapter 4

Needle Tracking and Trajectory Prediction

Prostate brachytherapy needles are typically 200 mm in length, and are often bevel-tipped so that the needle can slice through soft-tissue while still allowing the brachytherapy seeds to be easily ejected. The bevel causes an imbalance of forces applied to the needle tip as it cuts through tissue, causing the needle to deflect during insertion. These factors, when combined with the effects of tissue deformation, can lead to significant errors in needle placement if corrective steering is not performed [69].

Typically, during manual PPB surgery, the surgeon monitors a transverse US slice near the maximum insertion depth of the needle. Once the needle has been inserted, a cross-sectional view of the needle appears in the transverse image. If the needle is too far from the pre-planned target position as observed in the US image, the needle is withdrawn and inserted again until the placement error is within the surgeon's tolerance range. The surgeon's ability to steer the needle under limited feedback is critical for minimizing the number of re-insertions required and to deliver the prescribed dose distribution. However, there are no well-defined guidelines for needle steering for these type of procedures, with steering strategies normally developed through empirical

observation, experience, and trial-and-error.

4.1 Problem Formulation

In this chapter, we present a method to assist surgeons during needle insertion procedures by providing reliable needle tracking in US images and reducing movement of the US probe. This is demonstrated using a semi-automatic needle steering system. The needle insertion procedure is divided into two consecutive phases. In the first phase, the US probe and the needle move in tandem, such that the needle tip is constantly in the field of view of the US images. In order to track the needle in the US images, we developed a threshold-based image processing algorithm combined with Kalman filtering. Once the needle is located in the US images, the information is used to parameterize a kinematic, quasi-static needle-tissue interaction model that is used to estimate future needle tip deflection. The needle is rotated once the current tip deflection reaches a user-specified threshold. In the second phase of the insertion, the US probe stops while the needle continues to be inserted. This is to prevent the US probe from applying force to tissue and critical structures found at or near the target area. It is assumed that needle rotation occurs before the probe stops moving, and that a single rotation at an appropriate depth is used to correct the trajectory of the needle.

The contributions of this chapter include the development of a robust needle tracking method based on image processing, Kalman filtering and a needle-tissue interaction model that relies solely on 2D US feedback for parametrization without the need for tissue characterization. In addition, our method allows the US probe to be stopped at a desired depth in order to avoid tissue deformation caused by US probe contact. The method is demonstrated using biological tissue experiments and a basic threshold-based needle steering system. The rest of the chapter is organized as follows. In Section 4.2, the

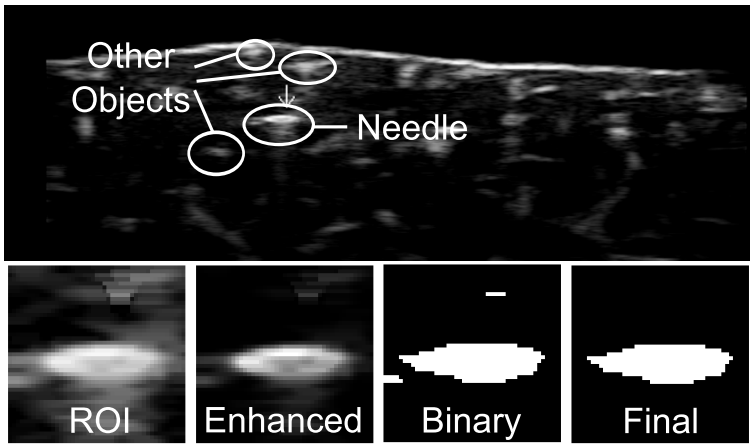

Figure 4.1: An image of the needle embedded within biological tissue. The needle and extraneous background objects are shown. Underneath, the image processing steps are shown.

needle-tracking algorithm is defined. The model for needle tip trajectory prediction is outlined in Section 4.3. In Section 4.4, the biological experiments and the experimental setup is described. Results are shown in Section 4.5 and are discussed in Section 4.6. Conclusions are summarized in Section 4.7.

4.2 Real-time Needle Tracking in US Images

In this section, the method for real-time needle tracking is described. Our setup continuously receives transverse US images of the needle. In transverse images, a cross-section of the needle is shown, such that the needle appears as a bright, elliptical object, as shown in Fig. 4.1.

4.2.1 Image Processing

The initial image processing method is based on our work described in Section 3.2. We first manually initialize a 2.5 mm by 2.5 mm ROI around the needle's starting position, as shown in the panel of Fig. 4.1 labelled ROI. Next, we apply contrast stretching using equation (3.1) introduced in Section 3.2.2 to

improve contrast between the bright needle pixels and the dark background tissue. An example of the enhanced ROI is shown in Fig. 4.1 in the panel labeled Enhanced. After enhancing the ROI, its cumulative histogram is used to determine an appropriate intensity threshold. The intensity threshold is similar to the one used in Section 3.2.3, but incorporates some slight improvements. The threshold is chosen based on the number of pixels n within the ROI expected to correspond to the needle, which is obtained from (4.1):

$$n = \frac{\beta A I_{max}}{I_{dx} I_{dy}} \tag{4.1}$$

where A is the area of the needle's cross section in mm^2, I_{dx} and I_{dy} represent the height and width dimensions of a single pixel in the ROI in mm, respectively, and β is a manually selected parameter used to account for needle distortion caused by attenuation, diffraction and diffusion of the US beam. In our work, β was set to 0.75 based on empirical tests. The intensity threshold selected for the ROI is that in which at least n pixels lie above the threshold. I_{max} is also used to modify the expected number of needle pixels. When I_{max} is low, the needle is less visible, and so the expected number of needle pixels is decreased to compensate. After the threshold is applied, the result is a binary image, as shown in Fig. 4.1 in the panel labelled Binary. After thresholding is completed, any cluster of needle point candidates with fewer than 20% of n connected components are removed. After all image processing steps have been performed, we obtain a set of needle point candidates as shown in Fig 4.1 in the panel labelled Final. A Kalman filtering algorithm is used to filter outliers from the set of candidate points, as well as deal with other issues described in the next section.

4.2.2 Kalman Filtering

The Kalman filter has been successfully used for needle tracking in [70, 71, 29, 72]. In this chapter, we use it not only to help improve the needle estimation, but to help remove outliers from the ROI, such as air bubbles, or tissue inhomogeneities, which can often be mistaken for the needle when performing multiple insertions into biological tissue. As well, sometimes whether due to loose contact between the probe and the tissue, or due to extreme attenuation of the needle, the needle appears with very poor visibility within the ROI such that it can not be found with the traditional image processing steps described above. The Kalman filter is used to predict where the needle should be within the ROI given the needle's historical trajectory. After Kalman filtering, the ROI for the next iteration is updated by centering the ROI around the updated needle position estimate. It is assumed that the change in needle tip position is constant between successive frames. The state prediction $\hat{\boldsymbol{x}}_{k|k-1}$ is the prediction of the needle tip position x and y and the change in tip position with respect to depth x' and y' at sample k given the state results from the previous iteration where the state $\boldsymbol{x}$ is:

$$\boldsymbol{x}_k = \begin{bmatrix} x_k \\ y_k \\ x'_k \\ y'_k \end{bmatrix} \tag{4.2}$$

The state prediction at sample k given the sample at $k-1$ is calculated as follows:

$$\hat{\boldsymbol{x}}_{k|k-1} = F\hat{\boldsymbol{x}}_{k-1} \tag{4.3}$$

where F is the state transition model used to calculate the state prediction. The state transition model is given by:

$$F = \begin{bmatrix} 1 & 0 & \Delta d & 0 \\ 0 & 1 & 0 & \Delta d \\ 0 & 0 & 1 & 0 \\ 0 & 0 & 0 & 1 \end{bmatrix} \tag{4.4}$$

where Δd represents the change in depth between successive US frames.

During cases where there are multiple objects present within the ROI, the state prediction $\hat{\boldsymbol{x}}_{k|k-1}$ is used to detect outliers. The needle location is estimated using (4.3). Any needle point candidates within a window of 110% of the outer needle diameter are considered inliers, and points outside of this window are ignored.

If the needle can be located within the ROI, the measured needle location $\mathbf{z_k}$ is obtained using (4.5).

$$\boldsymbol{z}_k = \begin{bmatrix} \text{med}(x_{in}) \\ \text{med}(y_{in}) \\ \frac{\Delta x_N}{\Delta d_N} \\ \frac{\Delta y_N}{\Delta d_N} \end{bmatrix} \tag{4.5}$$

where x_{in} and y_{in} are the inlying needle point candidates, med$(\cdot)$ is the median operator, d_N is the change in depth over the past N frames, and x_N and y_N are the change in tip positions along the x and y axes, respectively, over the past N frames. The median is used rather than the mean as another method to protect against outliers.

After obtaining the measurements $\mathbf{z_k}$ from the US images, the needle location is updated using the Kalman filter to obtain the updated state estimation $\hat{\boldsymbol{x}}_{k|k}$, based on the state vector results obtained from the previous iteration

using the following equation:

$$\hat{\boldsymbol{x}}_{k|k} = \hat{\boldsymbol{x}}_{k|k-1} + K_k \boldsymbol{z}_k \tag{4.6}$$

where K_k is the Kalman gain, which is related to the degree of correction caused by the incoming measurements $\mathbf{z_k}$. The Kalman gain is calculated using:

$$K_k = P_{k|k-1} H_k^T S_k^{-1} \tag{4.7}$$

where $\hat{\boldsymbol{P}}_{k|k-1}$ is the co-variance error of the state prediction $\hat{\boldsymbol{x}}_{k|k-1}$, H is the measurement model used to define the states that are being measured at each sample k, and S_k is the covariance of the residuals, which is related to the variability in $\mathbf{z_k}$. The equation for $\hat{\boldsymbol{P}}_{k|k-1}$ is given by:

$$\hat{\boldsymbol{P}}_{k|k-1} = F \hat{\boldsymbol{P}}_{k-1} F^T + Q \tag{4.8}$$

where Q is the process noise covariance matrix. The residual covariance S_k and the measurement model H are given by the following equations:

$$S_k = H_k P_{k|k-1} H_k^T + R \tag{4.9}$$

$$H_k = \left[\; I_{4\times 4} \; \right] \tag{4.10}$$

where R is the measurement noise covariance.

The end result of the Kalman filtering procedure is an improved estimation of the needle location based on the past observations of needle trajectory. The ROI for the next iteration of the needle tracking procedure is centered around this improved estimation of the needle tip position. In the event that the needle cannot be located within the ROI for brief periods of time, the state prediction $\hat{\boldsymbol{x}}_{k|k-1}$ is used to predict the needle location and update the ROI so that the needle can continue to be tracked once it reappears. In this case, the updated

state estimation $\hat{\boldsymbol{x}}_{k|k}$ is carried over from the previous iteration. In the event that multiple objects are present in the ROI, the state prediction $\hat{\boldsymbol{x}}_{k|k-1}$ is used to determine where the needle should be found within the ROI. Objects lying outside a radius of 110% of the needle's outer radius are considered to be outliers and are removed from the image.

4.3 Needle Modelling and Needle Tip Deflection Prediction

In addition to needle tracking, we require the ability to estimate the future needle tip deflection. As well, as discussed previously, in the second phase of our needle insertion procedure the probe is stopped while the needle continues to be inserted. In this situation, we need a model for estimating the current needle tip deflection along with the future tip deflection. Mechanics-based elastic beam models with virtual springs have been widely used for needle steering in [32, 24, 33, 34]. As well, a finite-element method with potential force-fields for needle steering and motion planning has been developed in [35, 36].

These models require accurate characterization of tissue, which is difficult to obtain during *in-vivo* procedures. Here, we propose a simple kinematic needle-tissue interaction model that can be completely parameterized using the US-based needle deflection feedback described in the previous section. Euler-Bernoulli beam theory is used in this chapter to identify forces applied to an elastic beam, from which the beam's shape can be identified.

The brachytherapy needle can be modelled as a hollow, cylindrical cantilever beam. The needle's deflection can be modeled as a beam with a point load applied to the tip to represent the cutting force applied to the bevel, and second point load applied to the middle of the length inserted into tissue to represent the force exerted by the tissue. An example is shown in Fig. 4.2.

The beam's shape can be derived from the bending moment $M(z)$ applied

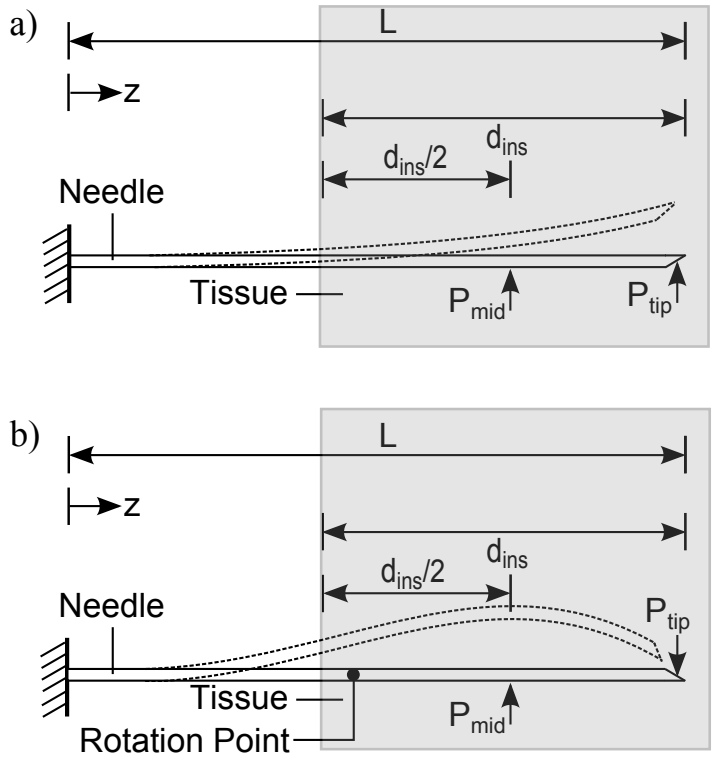

Figure 4.2: Needle shape modeling based on point loads applied to a cantilever beam. a) Needle shape before rotation. b) Needle shape after rotation. P_{tip} represents the force applied to the needle tip. P_{mid} represents the force applied to the middle of the inserted needle length.

at a distance z from the base of the beam. The bending moment equation is given by:

$$M(z) = EI\frac{d^2\delta}{dz^2} \tag{4.11}$$

where E is the modulus of elasticity of the beam, I is the area moment of inertia of the beam, and δ is the deflection of the beam at a distance z. For a beam with the point loads applied as in Fig. 4.2, $M(z)$ is equal to:

$$M(z) = P_{tip}(L - z) + P_{mid}\langle\alpha - z\rangle \tag{4.12}$$

where

$$\alpha = L - \frac{d_{ins}}{2} \tag{4.13}$$

P_{tip} and P_{mid} represent the forces applied to the needle tip and the centre of the inserted needle depth d_{ins} respectively, L is the needle length, and the function $\langle\cdot\rangle$ represents the singularity function:

$$\langle A - B\rangle = \begin{cases} 0, & \text{if} A \leq B \\ A - B, & \text{if} A > B \end{cases} \tag{4.14}$$

The integral of (4.12) is the slope $\theta(z)$ of the beam at a distance z:

$$\theta(z) = \frac{1}{2EI}[P_{tip}z(2L - z)] + \frac{1}{2EI}P_{mid}[\alpha^2 - \langle\alpha - z\rangle^2] \tag{4.15}$$

Integrating (4.15) allows us to solve for the deflection of the beam:

$$y(z) = \frac{1}{6EI}[P_{tip}z^2(3L - z) + P_{mid}(3\alpha^2 z - \alpha^3 + \langle\alpha - z\rangle^3)] \tag{4.16}$$

Assume that the beam deflection y_d and the slope θ_d at a distance $z = d$ along the beam is known from the US image processing algorithm described in the previous section and $d > \frac{d_{max}}{2}$, where d_{max} is the maximum insertion depth.

Then using (4.15) and (4.16), we can solve for P_{tip} and P_{mid}:

$$P_{tip} = 2EI \frac{3y_d + a\theta_d - 3d\theta_d}{d\left(2L\alpha - 3Ld - \alpha d + 2d^2\right)} \tag{4.17}$$

$$P_{mid} = \frac{P_{tip}d^2 - 2LP_{tip}d + 2\theta_d EI}{\alpha^2} \tag{4.18}$$

Using (4.16)-(4.18) we can solve for the needle's deflection along the beam. In our case, for the first phase of the insertion, when the US probe follows the needle tip, the deflection and slope at the needle tip is known. In the second phase of the insertion, when the US probe stops moving while the needle continues to be inserted, the deflection is known, and the slope at the observed depth is assumed to remain constant relative to the last measured slope obtained from the first phase.

In order to predict the tip trajectory at the maximum depth d_{max}, the beam is extrapolated by a length of a, where a is the difference between the maximum depth and the current depth of the needle. Before the needle is rotated (or in the case where no rotation occurs), the extrapolated segment of the beam is represented with a first-order polynomial with a slope equal to the slope of the needle tip. After rotation, due to the added flexion of the beam, the extrapolated segment of the beam is represented with a curve of constant radius, which is fitted to the portion of the beam found after the rotation depth.

The end result is a needle-tissue interaction model based on Euler-Bernoulli beam theory, which can be used for prediction of the needle tip position at the maximum depth. The model itself is parameterized solely using US image feedback, which is beneficial for *in-vivo* procedures, since there is no need to obtain tissue characteristics for each new patient.

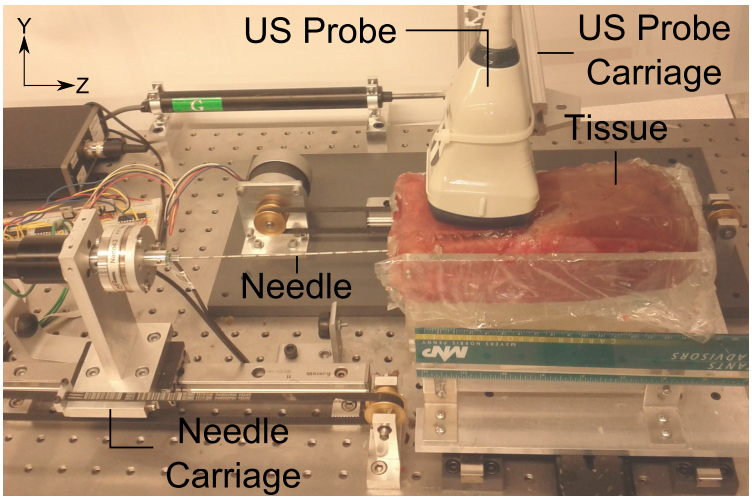

Figure 4.3: Needle insertion setup. The needle and probe are attached to separate motorized carriages. The probe moves with the same velocity as the needle up to a specified depth. Afterwards, the needle continues while the probe remains stationary.

4.4 Experimental Setup

We used a version of the the needle insertion device demonstrated in [73] for our needle insertion experiments. An image of the device is shown in Fig. 4.3. The needle is mounted on a two degree-of-freedom system consisting of a prismatic joint allowing for needle insertion along the z-axis and a revolute joint allowing for needle rotation about the z-axis. The prismatic joint is controlled with a Maxon RE40 DC motor and the revolute joint is controlled with a Maxon RE25 1:14 geared motor (Maxon Motor AG, Sachseln, Switzerland). The revolute joint is directly coupled to the motor, while the prismatic joint consists of a ball bearing-mounted carriage system attached to a motorized belt, which allows for control of the needle's insertion velocity. The motors are controlled with a Humusoft MF624 DAQ card which interfaces to a PC via PCI.

A separate prismatic joint is attached to a translating stage, which is used to mount the US probe. The joint is controlled through a separate motor, which allows the US probe to move independently of needle. The insertion

procedure can be separated into two consecutive phases. In the first phase, the needle can be inserted either manually or with a constant velocity. The velocity of the US probe is matched to the needle's velocity so that the needle tip is constantly observed in the US images. In the second phase, the velocity of the US probe carriage is set to zero while the needle continues to be inserted. This is to allow for monitoring of the needle without affecting movement of critical targets caused by force applied by the US probe. Fig. 4.4 shows how the velocity of the US probe is controlled during the different phases of the needle insertion procedure. The position of the needle carriage and the US probe are measured, and the velocities are controlled using a PID controller. During the first phase, the desired velocity of the US probe carriage is equal to the measured velocity of the needle carriage. During the second phase, the velocity of the US probe carriage is set to zero. If the needle is instead inserted manually, the PID controller is only used to control the US probe carriage.

US images are collected using a SonixTouch Ultrasound System (Analogic Ultrasound, Richmond, BC, Canada) and a linear US transducer model 4DL14-5/38 (Analogic Ultrasound, Richmond, BC, Canada). A DVI-to-USB 3.0 frame grabber (Epiphan, Palo Alto, CA, USA) transfers the images from the US machine to a PC for processing at a frame rate of 20 Hz.

The needle used for the experiments is an 18 gauge, bevel-tipped brachytherapy needle, model PSS1820EZ (Worldwide Medical Technologies, Oxford, CT, USA). Fresh, *ex-vivo* beef tissue was used for the offline experiments described in Section 4.5.1. For the online experiments described in Section 4.5.2, a beef tissue phantom with an initial 20 mm layer of gelatin to simulate the effects of multiple tissue layers and internal tissue interfaces was used. After consulting with brachytherapy surgeons, beef tissue was identified as being most similar from a surgeon's perspective to the clinical cases.

During the first phase of the insertion, the US probe follows the needle tip. The deflection of the needle tip is monitored via the US images. The needle

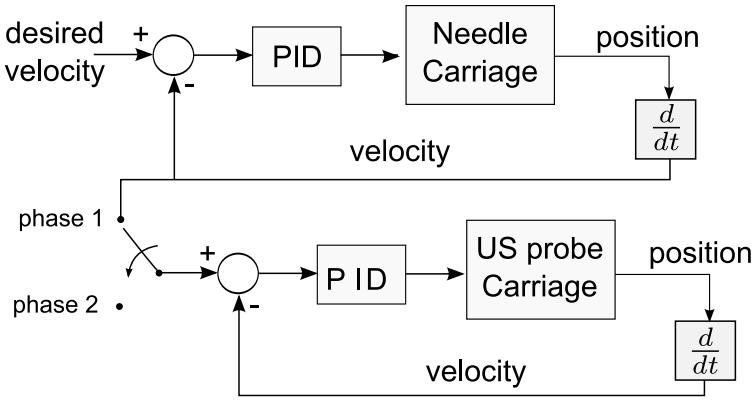

Figure 4.4: Block diagram showing how the US probe is controlled through phases 1 (where the probe follows the needle tip) and 2 (where the probe stops while the needle continues) of the needle insertion procedure.

rotates once the resultant magnitude of deflection in the x and y planes (δ_x and δ_y respectively) reaches a threshold ϵ. At this point, the needle rotates by an amount ϕ defined by (4.19):

$$\phi = 180^\circ + \arctan\left(\frac{\delta_y}{|\delta_x|}\right) \tag{4.19}$$

where $\phi = 0^\circ$ represents the angle where the needle bevel is aligned with the x plane such that needle deflection occurs in the $+x$ direction under ideal conditions. Before insertion begins, the needle is always aligned to the $\phi = 0^\circ$ position. Equation (4.19) allows us to counteract some of the minor out-of-plane deflection caused by tissue motion or insertion angle.

4.5 Experimental Results

First, we validated the needle tip prediction model using offline experiments, where the needle insertion velocity is controlled by the robot. Then, we performed online experiments where the needle is manually inserted, and a threshold-based controller is used to compensate for needle deflection once it reaches the

specified threshold.

4.5.1 Prediction of Needle Deflection

Offline experiments are performed with the probe positioned at the needle tip throughout the entire trial. Insertion trials without rotation are performed at constant velocities of 5, 10, 20, and 30 mm/s and insertion trials with rotation are performed at a constant velocity of 5 mm/s, with the needle being rotated after an insertion depth of 40 mm or 80 mm, for a total of 48 insertion trials all together. In all trials, the needles are inserted to a depth of 140 mm. The needle tip is tracked for each trial offline using the procedure outlined in Section 4.2 and the needle's trajectory is predicted using the equations developed in Section 4.3.

In the next section, we use a threshold-based controller to compensate for needle deflection in real-time.

4.5.2 Online Needle Tip Prediction and Steering

Preliminary experiments are shown in Fig. 4.6. As can be seen, the depth of rotation is a strong determinant of the final needle deflection. If the needle is rotated early during the needle insertion process such as at 40 mm, when the needle has not yet deflected a significant amount, the final tip deflection results in a 60% decrease in deflection compared to the case with no rotation. When the needle is rotated relatively late during insertion such as at 80 mm, the final needle tip deflection does not result in a significant difference compared to the case with no rotation. The needle must rotate relatively early during the insertion in order to have a noticeable impact on tip deflection. Therefore, the value for the deflection threshold ϵ must be relatively small in order to influence the tip deflection by a useful margin. We selected a deflection threshold of $\epsilon = 2$ mm to demonstrate how our needle deflection prediction method could

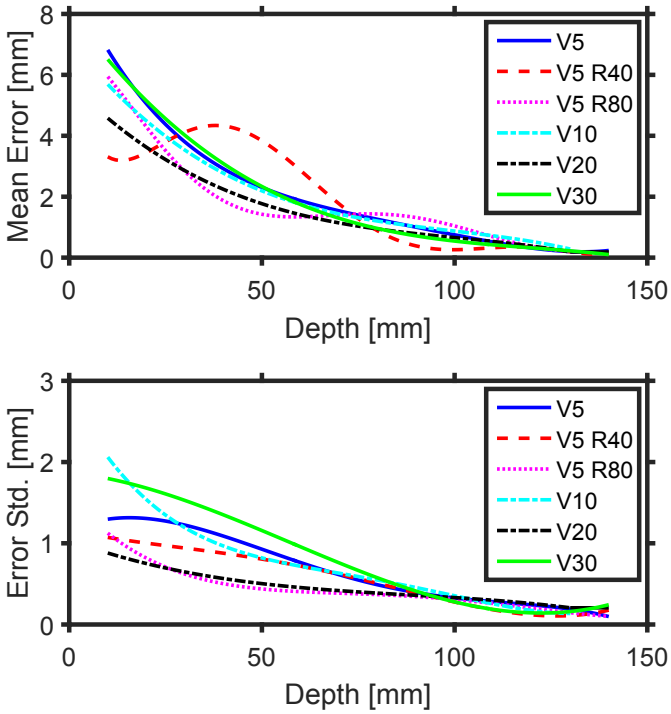

Figure 4.5: Comparison of the predicted needle tip deflection error relative to the actual final tip deflection as a function of the maximum depth observed by the US probe. The (a) mean and (b) standard deviation of the prediction error are shown.

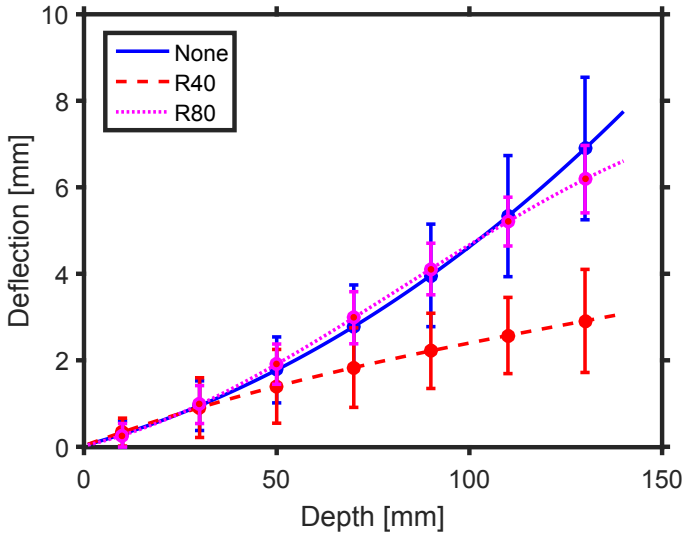

Figure 4.6: Comparison of needle tip deflection for cases with rotation at a depth of 40 mm (R40), 80 mm (R80) and without rotation (None). The needles were inserted at a velocity of 5 mm/s to a depth of 140 mm. The error bars show the standard deviation calculated for each case.

be integrated with a needle steering system. This threshold was chosen based on empirical results observed in test trials, as well as the results obtained in [74]. Future work will focus on developing more robust control algorithms for use with the deflection algorithm presented here.

Fifteen needle insertion trials are performed with steering and fifteen are performed without steering for a total of 30 trials in total. The tip deflection prediction results for each are compared. The needle is inserted manually to a depth of 140 mm. The US probe moved in tandem with the needle tip up to a depth of 90 mm, which was selected based on the results of the offline deflection experiments. For cases with needle steering, the needle rotates after a deflection threshold of $\epsilon = 2$ mm. Boxplot comparisons of the final tip deflection for the cases with and without needle steering are shown in Fig. 4.7. The use of steering decreased the final tip deflection from an average of 10 mm to an average of 3.7 mm.

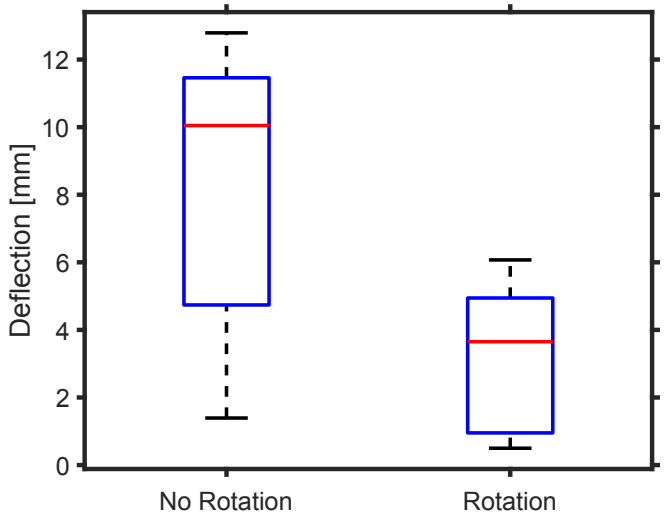

Figure 4.7: Comparison of the final tip deflection with respect to cases with no needle steering (No Rotation) and the cases with needle steering (Rotation).

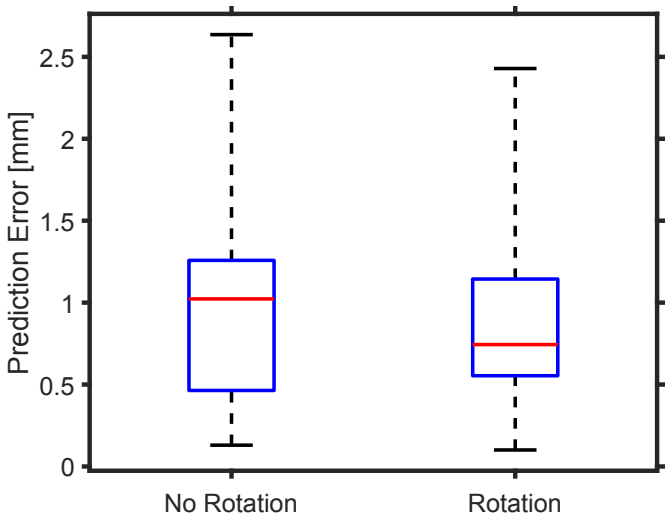

Figure 4.8: Comparison of the prediction error with respect to cases with no needle steering (No Rotation) and the cases with needle steering (Rotation). The prediction error represents the absolute difference between the final predicted needle tip deflection and the true tip deflection.

Boxplot comparisons of the prediction error between the predicted needle tip deflection at the end of the insertion and the actual needle tip deflection at the end of the insertion are shown in Fig. 4.8. For cases without rotation, the needle can be predicted with a median accuracy of 1.0 mm, with accuracies ranging from 0.1 mm to 2.6 mm. For cases with rotation, the needle can be predicted with a median accuracy of 0.7 mm, with accuracies ranging from 0.1 mm to 2.4 mm.

4.6 Discussion

Fig. 4.5 shows the error between the final predicted tip deflection and the actual tip deflection as a function of the US probe's final observed depth. V5, V10, V20 and V30 represent insertions performed at constant velocities of 5 mm/s, 10 mm/s, 20 mm/s, and 30 mm/s respectively. V5 R40 and V5 R80 represent insertions performed at a velocity of 5 mm/s with rotations performed at a depth of 40 mm and 80 mm respectively.

As observed in Fig. 4.5, both the mean and standard deviation of the prediction error generally decreases the longer that the needle tip is observed over the course of the insertion. When the needle tip is observed to a depth of 70 mm onwards, the needle tip deflection can be predicted with an accuracy of 1.8 ± 1.6 mm for all cases except the V5 R40 case. From depths of 90 mm onwards, the needle tip deflection can be predicted with an accuracy of 1.3 ± 1.0 mm for all cases. For cases with rotation, the needle must be observed at depths greater than the rotation depth in order to predict the tip deflection with an accuracy of less than 2 mm.

The online experiments show that the needle tip deflection can be predicted with an average error of less than 1.0 mm when the probe is stopped at a depth of 90 mm or 64% of the maximum insertion depth. These errors are smaller than the 5 mm placement accuracy of experienced physicians [75].

In current PPB practices, the probe is typically positioned at or near the desired insertion depth. The needle must be fully inserted before needle placement can be assessed. If the needle is placed too far from the target location, the needle must be withdrawn and re-inserted. This process of performing multiple re-insertions to obtain satisfactory needle placement can cause increased tissue trauma and swelling. By moving the US probe in tandem with the needle at the beginning of the insertion, the surgeon can accurately monitor the needle's deflection well before the maximum insertion depth. This allows them to decide well in advance of the maximum insertion depth whether a re-insertion would be necessary. In addition, through the use of an appropriate needle steering algorithm, the needle can be automatically rotated to consistently reduce needle tip deflection, preventing the need for re-insertions in the first place.

Stopping the US probe before the desired insertion depth at the second phase of the insertion procedure is highly beneficial, as tissue motion of the target area caused by force applied by the US probe is reduced. For transrectal US-guided procedures, the probe does not need to be inserted as far using the proposed method, which should help simplify the procedure by minimizing movement of the probe. This system holds great potential for US-guided percutaneous needle insertion procedures where the needle must travel a significant length into the body, such as prostate brachytherapy or biopsy of deep tissues.

Since the kinematic needle-tissue interaction model is parameterized solely based on US image feedback, the needle must be rotated before the probe stops moving, such that the needle tip's new trajectory can be properly estimated. This limitation is not overly restrictive however, since, based on Fig. 4.6, the needle must rotate early during the insertion process in order to have a significant impact on needle deflection. Another limitation is that the model currently accounts for single rotations, not multiple rotations.

4.7 Concluding Remarks

In this chapter, a method for automatic needle tracking in US images and needle tip deflection prediction is presented and is demonstrated with a semi-automatic needle steering system. A threshold-based image processing algorithm is combined with Kalman filtering to develop a robust needle tracking procedure for use with transverse US images. The needle tracking results are used to fully parameterize a needle-tissue interaction model. The model is then used to predict future tip deflection. The semi-automatic needle steering procedure is divided into two consecutive phases. In the first phase, the US probe is moved in tandem with the needle such that the needle tip is constantly in the field of view of the US images. In the second phase of the procedure, the US probe stops while the needle continues to be inserted in order to prevent the probe from applying unnecessary forces to deeper tissue and structures.

Results showed that for cases without rotation, the needle tip deflection can be predicted with an average accuracy of 1.0 mm, ranging from 0.1 mm to 2.6 mm. For cases with rotation, the needle can also be predicted with an average accuracy of 0.7 mm, ranging from 0.1 mm to 2.4 mm.

This system can be of great aid to surgeons performing deep percutaneous needle insertion procedures such as prostate brachytherapy. In the first phase of the procedure, the US feedback can provide information for the surgeon about future tip deflection so that they can determine the accuracy of the needle placement. In the second phase of the procedure, the US probe can be stopped to prevent applying tissue forces to the target area while providing the surgeon with an accurate estimation of the current and future needle tip deflection.

Chapter 5

Needle Steering

Bevel-tipped needles are useful in the sense that they are easy to manufacture and can be designed with a hollow interior to allow for drugs or fluids to be ejected from the needle [76]. The design also allows the needle to maintain a sharp tip that can be effectively advanced through multiple tissue layers. However, the bevel results in an asymmetrical tip which leads to an imbalance of tip forces [77, 78, 79], which causes the needle to deflect during the insertion process. A depiction of the forces applied to the needle tip during insertion is shown in Fig. 5.1.

Surgeons using bevel-tipped needles to perform deep-tissue percutaneous needle insertion procedures, like PPB, must perform corrective needle steering in order to guide the needle towards its target location. Strategies for needle steering are often only developed through personal experience, and trial-and-error, making it a very difficult skill for new practitioners to learn.

5.1 Problem Formulation

In this chapter, we demonstrate a 3D needle steering algorithm based on the kinematic model of a flexible, bevel-tipped needle developed by Webster *et al.* [80], and developed in its current form by Kallem and Cowan [37]. The in-

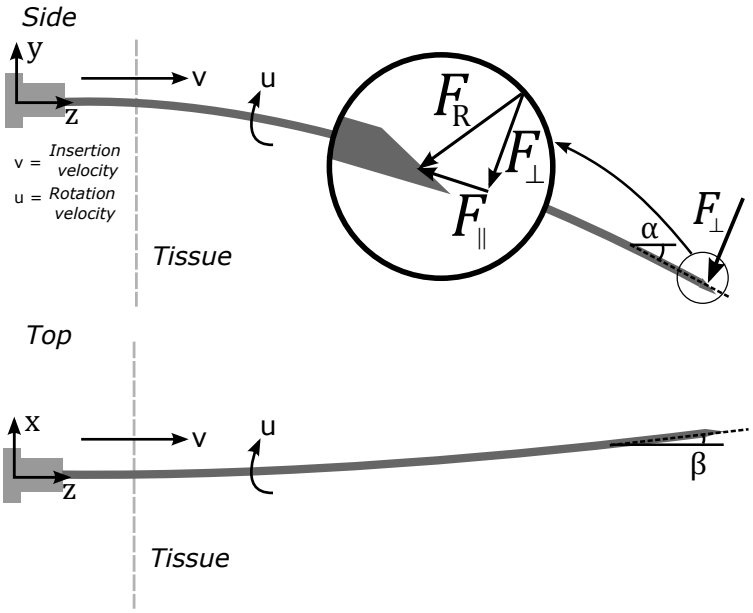

Figure 5.1: Bevel-tipped needle forces. F_R represents the tissue cutting force. $F_\parallel$ and $F_\perp$ represents the component forces parallel and perpendicular to the deflected needle shaft, respectively.

tent is to develop a robotic needle steering assistant that can help surgeons perform corrective needle steering during percutaneous needle insertion procedures. This type of technology would be very beneficial to new surgeons who do not yet have the skill and experience to achieve consistent needle insertion results.

Integrator-backstepping was used to design the control inputs for our two planar needle steering methods, which are combined to control the needle's 3D tip path. Integrator-backstepping is a nonlinear design tool based on proper selection of a Lyapunov function. The main premise is to divide the system into multiple cascaded subsystems which are easier to solve and fine-tune. Then, we gradually work back towards the original system to obtain the final controller design. The proposed controller design will be discussed in further detail in Section 5.2.

The main contribution of this chapter includes a needle steering control design that attempts to reduce deflection in both the $x - z$ and $y - z$ planes

without requiring continuous rotation like many other steering methods. Instead, our method focuses on making smaller-scale, slower rotations throughout the insertion process to minimize deflection. This is beneficial because it avoids requiring the needle to "drill" into tissue. The relationship between continuous needle rotation, tissue trauma, and tissue recovery is not well-understood and from a clinical perspective, it is sensible to avoid tissue damage as much as possible. Further analysis of tissue trauma is performed in Section 5.4.1.

The rest of the chapter is structured as follows. Section 5.2 describes the derivation of our steering algorithm and controller design. In Section 5.3, the needle steering robot used in this chapter is shown, and an illustration of our experimental setup is provided. Simulation and experimental results are shown in Section 5.4 and in Section 5.5, the results are detailed and discussed. Conclusions are drawn in Section 5.6.

5.2 Integrator-Backstepping Controller

In this section, we discuss the development of our steering controllers derived using the nonlinear design technique known as integrator-backstepping. Our strategy makes use of two separate controllers, each designed to limit the needle's deflection to a single plane. By properly shifting between these two controllers, we can limit the needle's overall 3D deflection. In Section 5.2.1, we give a general overview of the integrator-backstepping technique applied in our needle steering application. In Section 5.2.2 we discuss the controller designed to limit needle deflection to the vertical plane, called Vertical Deflection Control. In Section 5.2.3, we discuss the controller designed to limit needle deflection to the horizontal plane, called Horizontal Deflection Control. In Section 5.2.4 we discuss the control logic for dealing with discontinuous points as well as for shifting between VDC and HDC.

5.2.1 Needle Steering Control Using Integrator-Backstepping

The kinematic model for a flexible bevel-tipped needle used in this chapter were based on the bicycle model developed by Webster *et al.* [80] and derived in its current-form in by Kallem and Cowan [37]. The kinematic model equations are shown below.

$$\begin{bmatrix} \dot{\boldsymbol{x}} \\ \dot{\boldsymbol{y}} \\ \dot{\boldsymbol{z}} \\ \dot{\boldsymbol{\alpha}} \\ \dot{\boldsymbol{\beta}} \\ \dot{\boldsymbol{\gamma}} \end{bmatrix} = \begin{bmatrix} \sin\beta & 0 \\ -\cos\beta\sin\alpha & 0 \\ \cos\alpha\cos\beta & 0 \\ \kappa\cos\gamma\sec\beta & 0 \\ \kappa\sin\gamma & 0 \\ -\kappa\cos\gamma\tan\beta & 1 \end{bmatrix} \begin{bmatrix} v \\ u \end{bmatrix} \tag{5.1}$$

The values x, y, and z refer to the position of the needle tip, while α, β, and γ refer to the yaw, pitch and roll of the needle respectively. The bevel orientation shown in Fig. 5.1 is at $\gamma = 0°$. The dot operator $\{\dot{}\}$ represents the first derivative with respect to time. The needle deflects along a curve defined by a radius of curvature κ. The values v and u refer to the insertion velocity and axial rotation velocity of the needle respectively, both of which are applied to the base of the needle by our needle steering robot. The variable u is the control input, and we assume that $v > 0$, since (5.1) is only valid for forward insertion of the needle, as opposed to needle retraction [80]. In this particular study v is held constant throughout the entire insertion.

In the integrator-backstepping approach, a stabilizing control input can be found for a system of the form

$$\dot{x} = f_0(x) + g_0(x)\xi_1 \tag{5.2}$$

$$\dot{\xi}_1 = f_1(x, \xi_1) + g_1(x, \xi_1)\xi_2 \tag{5.3}$$

$$\dot{\xi}_2 = f_2(x, \xi_1, \xi_2) + g_2(x, \xi_1, \xi_2)u \tag{5.4}$$

where x, ξ_1 and ξ_2 represent the state variables and u represents the control input.

A control law that stabilizes the above system to the origin can be derived in three steps, described in [81].

Step 1: Start with (5.2). Viewing ξ_1 as the input, we design the feedback control $\xi_1 = \phi(x)$ to stabilize (5.2) to the origin $x = 0$ and such that the Lyapunov function $V_0(x)$ is positive definite and radially unbounded, and $\dot{V}_0(x)$ is at least negative semi-definite.

Step 2: Consider the subsystem composed of (5.2) and (5.3). A stabilizing control law and the associated Lyapunov function $V_1(x, \xi_1)$ for this subsystem is given by the following equations

$$\phi(x, \xi_1) = \frac{1}{g_1}\left[\frac{\partial \phi(x)}{\partial x}[f_0(x) + g_0(x)\xi_1] - \frac{\partial V_0}{\partial x}g_0(x) - k[\xi_1 - x] - f_1\right] \quad (5.5)$$

$$V_1(x, \xi_1) = V_0(x) + \frac{1}{2}[\xi_1 - \phi(x)]^2 \quad (5.6)$$

where k is a tunable gain parameter, with $k > 0$.

Step 3: Now, consider the system composed of (5.2)-(5.4). A stabilizing control law and the associated Lyapunov function $V_2(x,\ \xi_1,\ \xi_2)$ is given by the following equations

$$u = \frac{1}{g_2}\left\{\frac{\partial \phi(x, \xi_1)}{\partial x}(f_0 + g_0\xi_1) + \frac{\partial \phi(x, \xi_1)}{\partial \xi_1}(f_1 + g_1\xi_2) - \frac{\partial V_1}{\partial \xi_1}g_1 - k\left[\xi_2 - \phi(x, \xi_1)\right] - f_2\right\} \quad (5.7)$$

$$V_2 = V_1 + \frac{1}{2}[\xi_2 - \phi(x, \xi_1)]^2 \quad (5.8)$$

These steps will now be applied to construct the VDC and HDC controllers.

5.2.2 Vertical Deflection Control (VDC)

In order to limit the needle to the vertical plane, thereby reducing deflection along the x-axis, we must develop a control input that brings $(x,\ \beta,\ \gamma) = (0,\ 0,\ 0)$. This can be performed by applying integrator-backstepping to the following subsystem:

$$\dot{x} = v \sin\beta \tag{5.9}$$

$$\dot{\beta} = \kappa v \sin\gamma \tag{5.10}$$

$$\dot{\gamma} = -\kappa v \cos\gamma \tan\beta + u \tag{5.11}$$

Let us use the change of variable $\xi_1 = \sin\beta$ and $\xi_2 = \sin\gamma$. Then we can re-write (5.9)-(5.11) as

$$\dot{x} = v\xi_1 \tag{5.12}$$

$$\dot{\xi}_1 = \pm\kappa v \left(\sqrt{1-\xi_1^2}\right)\xi_2 \tag{5.13}$$

$$\dot{\xi}_2 = \mp\frac{\kappa v \xi_1(1-\xi_2^2)}{\sqrt{1-\xi_1^2}} \pm \left(\sqrt{1-\xi_2^2}\right)u \tag{5.14}$$

The above system is now in strict feedback form. Now, we can begin deriving the control law to stabilize the system to the origin.

Step 1: Start with (5.12). Choosing the Lyapunov function $V_{0x}(x) = \frac{1}{2}x^2$, which is positive definite and radially unbounded, we can select $\xi_1 = \phi(x) = -x$ to stabilize (5.12) to the origin. Then $\dot{V}_{0x}(x) = -vx^2$ which is negative definite.

Step 2: Next, consider the subsystem composed of (5.12) and (5.13). Performing the change of variables $\rho = \xi_1 + x$ we obtain the following subsystem:

$$\dot{x} = v(\rho - x) \tag{5.15}$$

$$\dot{\rho} = v(\rho - x) \pm \kappa v \left(\sqrt{1-(\rho-x)^2}\right)\xi_2 \tag{5.16}$$

Selecting a Lyapunov function using (5.6), we obtain:

$$V_{1x} = \frac{1}{2}x^2 + \frac{1}{2}\rho^2 \tag{5.17}$$

$$\dot{V}_{1x} = -v\left[x^2 - \rho^2 \pm \kappa\rho\left(\sqrt{1-(\rho-x)^2}\right)\xi_2\right] \tag{5.18}$$

Viewing ξ_2 as an independent input for the subsystem in (5.15)-(5.16), we can find a state feedback control law $\xi_2 = \phi(x,\rho)$ to stabilize the subsystem to the origin. With respect to (5.15) and (5.16), a stabilizing control law can be selected using (5.5)

$$\phi(x,\xi_1) = -k_1\frac{\rho}{\pm\kappa\sqrt{1-\xi_1^2}} \tag{5.19}$$

where $k_1 > 1$.

Step 3: Using (5.7), and performing the substitutions $\pm\sqrt{1-\xi_1^2} = \cos\beta$ and $\pm\sqrt{1-\xi_2^2} = \cos\gamma$, a stabilizing control law u_x for the subsystem described in (5.9)-(5.11) can be written as

$$u_x = -\frac{v}{\cos\gamma}\left(\frac{k_1\tan\beta}{\kappa} + \frac{k_1\sin\gamma}{\cos^2\beta} + \kappa\cos\beta(\sin\beta + x) + \right.$$
$$\left.\frac{k_2}{v}\left[\sin\gamma + \frac{k_1(\sin\beta+x)}{\kappa\cos\beta}\right] - \kappa\cos^2\gamma\tan\beta\right) \tag{5.20}$$

where $k_2 > 0$. The corresponding Lyapunov function is

$$V_{2x} = \frac{1}{2}x^2 + \frac{1}{2}(\sin\beta + x)^2 + \frac{1}{2}\left(\sin\gamma + \frac{k_1(\sin\beta+x)}{\kappa\cos\beta}\right)^2 \tag{5.21}$$

Note that in (5.21) there are discontinuities at $\beta = \{90^\circ \pm (180^\circ)n,\ n \in \mathbb{N}\}$. In Section 5.2.4, we discuss the meaning of the discontinuities encountered in (5.20) and develop a revised control logic to handle these special cases, specifically, values of γ that cause (5.20) to diverge towards infinity.

5.2.3 Horizontal Deflection Control (HDC)

Analogous to the previous section, a similar strategy is used to develop a controller that limits the needle to the horizontal plane. We apply integrator-backstepping to the following subsystem:

$$\dot{y} = -v\cos\beta\sin\alpha \tag{5.22}$$

$$\dot{\alpha} = \kappa v\cos\gamma\sec\beta \tag{5.23}$$

$$\dot{\gamma} = -\kappa v\cos\gamma\tan\beta + u \tag{5.24}$$

Lyapunov methods stabilize systems about the origin. However, the steady-state conditions of (5.22)-(5.24) requires $(y,\ \alpha,\ \gamma) = (0,\ 0,\ 90^\circ)$. Therefore, we perform a simple change-of-variables by setting $\gamma' = \gamma - 90^\circ$ to transform (5.22)-(5.24) into the form:

$$\dot{y} = -v\cos\beta\sin\alpha \tag{5.25}$$

$$\dot{\alpha} = -\kappa v\sin\gamma'\sec\beta \tag{5.26}$$

$$\dot{\gamma} = \kappa v\sin\gamma'\tan\beta + u \tag{5.27}$$

Next, let $\zeta_1 = \sin\alpha$ and $\zeta_2 = \sin\gamma'$. Then, we can rewrite (5.25)-(5.27) as

$$\dot{y} = -v\left(\cos\beta\right)\zeta_1 \tag{5.28}$$

$$\dot{\zeta_1} = \pm\kappa v\sec\beta\left(\sqrt{1-\zeta_1^2}\right)\zeta_2 \tag{5.29}$$

$$\dot{\zeta_2} = \mp\kappa v\zeta_2\tan\beta\sqrt{1-\zeta_2^2} \pm \left(\sqrt{1-\zeta_2^2}\right)u \tag{5.30}$$

The above system is now in strict feedback form. Assume that β is known, either through measuring, modeling or using an observer. Now, we begin deriving the control law to stabilize the system to the origin $(y,\ \alpha,\ \gamma') = (0,\ 0,\ 0)$.

Step 1: Start with (5.28). Choosing the Lyapunov function $V_{0y}(y) = \frac{1}{2}y^2$,

which is positive definite and radially unbounded, we can select $\zeta_1 = \psi(y) = y$ to stabilize (5.28) to the origin. Then $\dot{V}_{0y}(y) = -v\,(\cos\beta)\,y^2$, which is negative definite assuming $\{\beta \in (-90°, 90°)\}$. In this study, corrective steering will be performed long before $\beta = \pm 90°$, so this assumption will be valid.

Step 2: Next, consider the subsystem composed of (5.28) and (5.29). Performing the change of variables $\eta = \zeta_1 - y$, we obtain the following subsystem:

$$\dot{y} = -v\cos\beta(\eta + y) \tag{5.31}$$

$$\dot{\eta} = v\cos\beta(\eta + y) \pm \kappa v \sec\beta\left(\sqrt{1-(\eta+y)^2}\right)\zeta_2 \tag{5.32}$$

Selecting a Lyapunov function using (5.6), we obtain

$$V_{1y} = \frac{1}{2}y^2 + \frac{1}{2}\eta^2 \tag{5.33}$$

$$\dot{V}_{1y} = -v\left[y^2\cos\beta - \left(\eta^2\cos\beta \mp \kappa\eta\zeta_2\sec\beta\sqrt{1-(\eta+y)^2}\right)\right] \tag{5.34}$$

Viewing ζ_2 as an independent input for the system in (5.31)-(5.32), we can find a state feedback control law $\zeta_2 = \psi(y, \eta)$ to stabilize the system to the origin $(y, \alpha, \gamma') = (0, 0, 0)$. With respect to (5.31)-(5.32), a stabilizing control law can be selected using (5.5)

$$\psi(y, \zeta_1) = \mp l_1 \frac{\eta\cos\beta}{\kappa\sqrt{1-(\eta+y)^2}} \tag{5.35}$$

where $l_1 > 1$. *Step 3*: Using (5.7), and performing the substitutions $\pm\sqrt{1-\zeta_1^2} = \cos\alpha$ and $\pm\sqrt{1-\zeta_2^2} = \cos\gamma'$, a stabilizing control law u_y for the system described in (5.28)-(5.30) can be written as

$$u_y = \frac{-v}{\cos\gamma'}\left(\frac{l_1\cos^2\beta\tan\alpha}{\kappa} + \frac{l_1\sin\gamma'}{\cos^2\alpha} + \frac{\kappa\cos\alpha(\sin\alpha - y)}{\cos\beta} + \frac{l_2}{v}\left[\sin\gamma' + \frac{l_1\cos\beta(\sin\alpha - y)}{\kappa\cos\alpha}\right] - \kappa\tan\beta\cos\gamma'\sin\gamma'\right) \tag{5.36}$$

where $l_2 > 0$. The corresponding Lyapunov function is:

$$V_{2y} = \frac{1}{2}y^2 + \frac{1}{2}(\sin\alpha - y)^2 + \frac{1}{2}\left(\sin\gamma' + \frac{l_1\cos\beta}{\kappa\cos\alpha}(\sin\alpha - y)\right)^2 \qquad (5.37)$$

Note that in (5.37) there are discontinuities at α (and β) $= \{90^\circ \pm (180^\circ)n,\ n \in \mathbb{N}\}$. In Section 5.2.4, we discuss the meaning of the discontinuities encountered in (5.20) and (5.36), and we develop a revised control logic to handle these special cases, specifically, values of γ that cause (5.20) to diverge towards infinity. We will also discuss how our proposed 3D needle steering method shifts between the HDC and VDC controllers described above.

5.2.4 Control Logic

The VDC and HDC controllers are combined to minimize the 3D deflection of the needle tip. Here, we will describe the way this is performed. First, based on the control laws derived in (5.20) and (5.36), we need to develop strategies to handle points like γ (or γ') $= \{90^\circ \pm (180^\circ)n,\ n \in \mathbb{N}\}$ and α (and/or β) $= \{90^\circ \pm (180^\circ)n,\ n \in \mathbb{N}\}$ where the control law tends towards infinity. With respect to α and β, these discontinuities occur when the needle's orientation is perpendicular to the $x - z$ and $y - z$ plane, respectively. In practice, we want to perform corrective actions long before the needle reaches this state, so this issue is not likely to occur and is not of great concern, especially with the 18 gauge brachytherapy needles used in our study. Of greater importance is the issue with γ (and γ'); discontinuities occur whenever the needle's bevel position aligns with the $x - z$ plane (or $y - z$ plane with respect to γ'). We have developed a strategy to handle situations where the control law guides γ towards these discontinuities.

We monitor γ, assuming that the bevel position of the needle's tip is the same as that of the needle's base. This assumption disregards the effects of torsional friction applied to the needle shaft, which should be quite small in

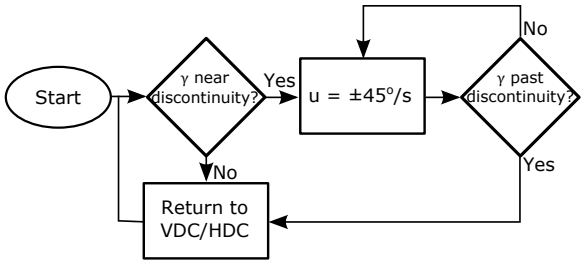

Figure 5.2: Discontinuity logic flowchart used during instances where γ is near discontinuities.

practice [80]. As long as γ is outside of 10° of one of the discontinuities, u is controlled via the equation (5.20) in the case of VDC or (5.36) in the case of HDC. If γ is within 10° of one of the discontinuities, we simply apply a constant $u = \pm 45^\circ$ to push γ to 10° past the discontinuity and re-apply the appropriate VDC or HDC control law. For example, if we are currently implementing VDC and γ approaches 80°, u is controlled to bring γ to 100° and (5.20) is re-instated. A summary of the control logic is shown in Fig. 5.2.

In switching between the VDC and HDC controllers, we monitor the deflections along the x and y axes. If the deflection along x is greater than y, we perform VDC. If the deflection along y is greater than x, we perform HDC. The radius of curvature κ limits the rate at which the deflection can be corrected. This imposes a natural delay between switching from one controller to another, preventing chattering, or unnecessarily high-frequency switching between HDC and VDC.

5.3 Experimental Setup

In this section, we will discuss our needle steering device, our ultrasound (US) setup, as well as the tissue phantoms used in our experiments.

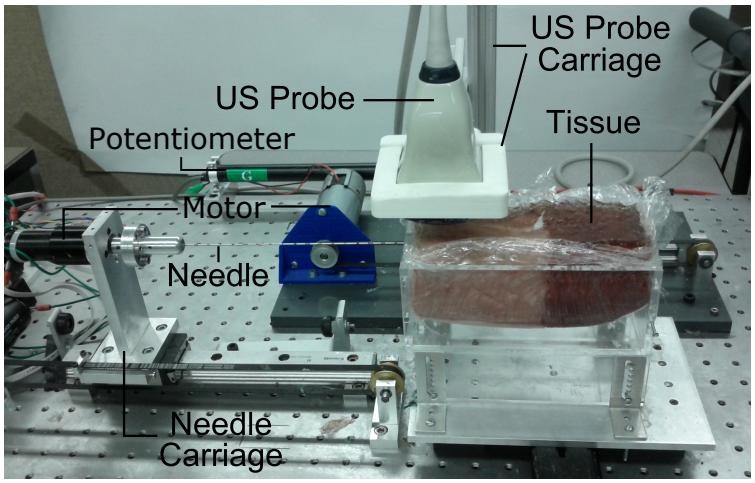

Figure 5.3: Needle steering device. A two degree-of-freedom needle insertion robot is used in our experiments. A prismatic joint which controls the needle's insertion velocity is attached to a needle carriage. A rotational joint controls the needle's axial rotation velocity. An US probe is attached to a separate motor and is used to track the needle tip over the course of the insertion. A potentiometer is used to determine the position of the US probe.

5.3.1 Needle Steering Device

Our needle steering device consists of a two degree-of-freedom robot, modified from the version described in [73]. A prismatic joint is used to control the needle's insertion velocity while a rotational joint is used to control the needle's axial rotation velocity, allowing us to adjust the needle's bevel angle during the insertion process. The axial rotation velocity is the input used for our needle steering controllers described in Section 5.2. The prismatic joint used to control the insertion velocity is designed using a ball-bearing mounted needle carriage system attached to a transmission belt. The transmission belt is connected to a Maxon RE40 DC motor (Maxon Motor AG, Sachseln, Switzerland), which controls the needle's linear motion. The revolute joint used to adjust the rotation velocity is powered by a Maxon RE25 1:14 geared motor (Maxon Motor AG, Sachseln, Switzerland). The motors are controlled through Simulink using a Humusoft MF624 DAQ card which interfaces with our PC via PCI connection. An image of the needle steering device is shown in Fig. 5.3.

A separate motorized prismatic joint is attached to an US probe holder whose position is monitored using a linear potentiometer. The US probe is controlled such that the needle tip is always in view of the US images. The US probe is positioned such that transverse images of the needle are obtained.

5.3.2 US Tracking

In order to track the needle under US feedback, we implemented the image processing algorithm described in Section 4.2.

US images are obtained with a SonixTouch Ultrasound System (Analogic Ultrasound, Richmond, BC, Canada) using a linear US transducer model 4DL14-5/38 (Analogic Ultrasound, Richmond, BC, Canada). The US machine is connected to a PC through a A DVI-to-USB 3.0 frame grabber (Epiphan, Palo Alto, CA, USA). The frame grabber obtains US images at a frequency of 20 Hz which are processed using Simulink.

5.3.3 Tissue Phantom

In our experiments, we used a dual-layer biological tissue phantom to test the effects of our needle steering control approach. The first 100 mm of the tissue phantom is composed of *ex-vivo* pork tissue while the final 70 mm of the phantom is composed of *ex-vivo* beef tissue. This design is intended to simulate the effects of multiple heterogeneous tissue layers that would be encountered during clinical PPB surgeries. A small layer of gelatin is added to the top of the dual-layer tissue phantom to provide a smooth, consistent surface on which the US probe can slide and to ensure good acoustic contact between the US probe and the tissue. An 18 gauge brachytherapy needle was used for each of the insertion trials. The needle's insertion velocity was held constant at 10 mm/s and the rotation velocity was limited to a maximum of $\pm 180°/s$.

5.4 Results

The first controller we are testing involves utilizing the VDC controller shown in (5.20) to minimize deflection along the x-axis in tandem with a threshold-based 180° switching algorithm to reduce deflection along the y-axis. The switching algorithm applies a 180° rotation whenever the deflection along the y-axis becomes greater than 1 mm. This threshold was based on results obtained in [74].

We also test a 3D steering method, swapping between (5.20) and (5.36) to reduce overall needle deflection. Whenever the deflection along the x-axis becomes greater than or equal to that along the y-axis, VDC is implemented. Whenever the deflection along the y-axis is greater than that along the x-axis, HDC is implemented.

In Section 5.4.1, we demonstrate through simulation that our 3D needle steering approach can achieve similar results to a constant rotation approach while causing much less tissue trauma. In Section 5.4.2 we use a multi-layered heterogeneous tissue sample to compare via experiments how the switching-based algorithm compares to the 3D steering method that incorporates both (5.20) and (5.36).

5.4.1 Simulation Results

Simulations are performed in Simulink to test the effects of various needle steering controllers on tissue trauma. Tissue trauma is obtained by measuring the amount of energy and friction-induced heat to which the tissue is subjected based on the amount that the needle is rotated throughout the insertion period. In our simulations, the insertion velocity v is set to 10 mm/s. The rotational velocity u is limited to a maximum of $\pm 180°/s$, except during the 180° switches implemented during the switching algorithm, where we allow the rotational velocity to increase to 360°/s. This increased rotational velocity is simply

to reduce the time spent performing the switch and increase the time spent implementing the VDC controller. The maximum insertion depth D is set to 140 mm. As well, the simulations were performed using $\kappa = 1/r$, with $r = 500$ mm. This is the typical deflection/curvature observed in preliminary *ex-vivo* biological tissue trials performed in our lab using an 18 gauge brachytherapy needle. In practice, the radius of curvature that defines the needle's deflection trajectory has been a well-studied topic [80, 37, 34], and can, in general, always be found.

We measure tissue trauma using the following equation:

$$\int_0^D u^2 dz \tag{5.38}$$

where D is the maximum insertion depth. A graph showing the simulated absolute deflection results versus depth as well as normalized comparison results of tissue trauma versus depth for the various controller designs is shown in Fig. 5.4. As shown in Fig. 5.4, our proposed method reduces the tissue trauma statistic by more than 50% over the constant rotation method. While the switching method performed the best with respect to tissue trauma, the switching method's ability to minimize the deflection throughout the insertion process is the worst of these three methods. Our proposed method can achieve improved deflection reduction over the other methods while yielding only a slightly higher tissue trauma statistic than the "Switching" approach. In the next section, we will compare the above switching method with the proposed 3D needle steering method using *ex-vivo* biological tissue phantoms.

5.4.2 Experimental Results

Here, we demonstrate how (5.20) can be combined with a simple switching-based algorithm, and we compare this to the use of a 3D steering approach which incorporates (5.20) and (5.36) in tandem. Our "switching"-based demon-

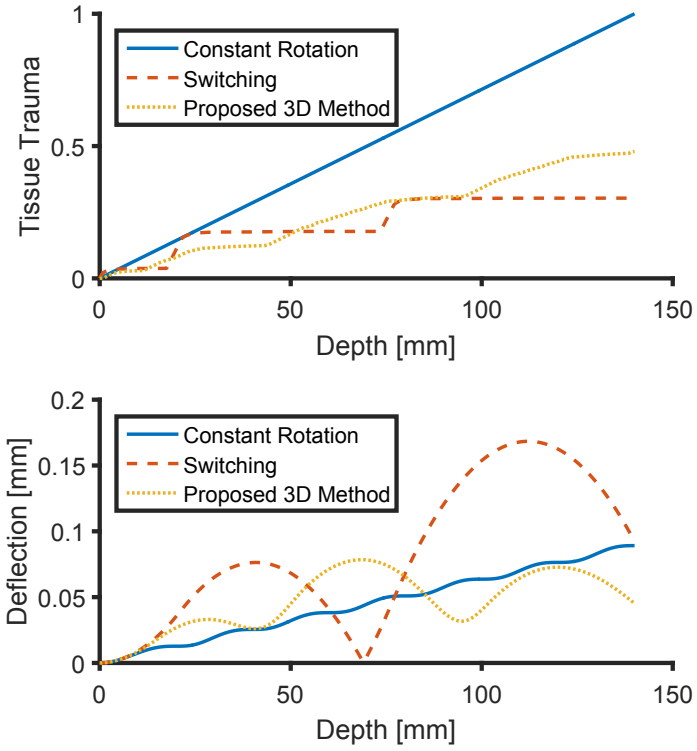

Figure 5.4: Simulation Results. The comparison of a) tissue trauma for different and b) 3D deflection for the different needle steering methods is shown. The needle's initial bevel position γ was set to 90° for each simulation and the remaining position/orientation values were initialized to 0.

Table 5.1: Comparison of Deflection Results in millimeters

Bevel Angle	**No Rotation**			**Switching**		
	x	y	**Total**	x	y	**Total**
0	1.3	11.9	12.0	0.2	3.5	3.5
45	9.6	14.5	17.4	0.5	2,1	2.1
90	8.2	4.9	9.6	0.2	0.7	0.7
135	7.6	2.1	7.9	0.3	3.3	3.3
180	1.4	8.5	8.7	0.4	3.6	3.6
225	8.2	3.8	9.1	1.0	3.7	3.8
270	11.1	2.8	11.5	0.4	1.8	1.8
315	10.6	7.9	13.2	0.7	2.6	2.7
Avg:	7.3	7.1	11.2	0.4	2.7	2.7

Bevel Angle	**Proposed Method Set 1**			**Proposed Method Set 2**		
	x	y	**Total**	x	y	**Total**
0	0.1	0.7	0.7	0.3	0.5	0.6
45	0.1	0.4	0.4	0.7	0.4	0.8
90	0.1	0.5	0.5	0.6	0.1	0.6
135	0.5	1.2	1.3	0.4	0.5	0.6
180	0.3	0.5	0.6	0.7	1.0	1.2
225	0.1	0.4	0.4	2.5	0.1	2.5
270	2.2	1.9	2.9	1.2	1.0	1.5
315	0.7	2	2.2	0.4	0.4	0.6
Avg:	0.5	1.0	1.1	0.9	0.5	1.1

stration uses the controller defined in 5.20 and rotates the needle 180° whenever the deflection along the y-axis is greater than 1 mm.

Using the multi-layered heterogeneous tissue sample described in Section 5.3.3, we compare the switching-based controller (labelled as "Switching" trials) to our 3D steering controller (labelled as "Proposed Method" trials) using a variety of needle bevel starting positions. A needle bevel angle of 0° represents the case where the needle bevel is aligned with the $y-z$ plane, as shown in Fig. 5.1. We test these controllers at bevel angle increments of 45° starting from 0° and ending at 315° to obtain 8 different bevel angle starting conditions in total. We also show how these controllers compare to insertion without needle rotation, which we label as "No Rotation" trials.

Both of the "No Rotation" and "Switching" trials are performed once at

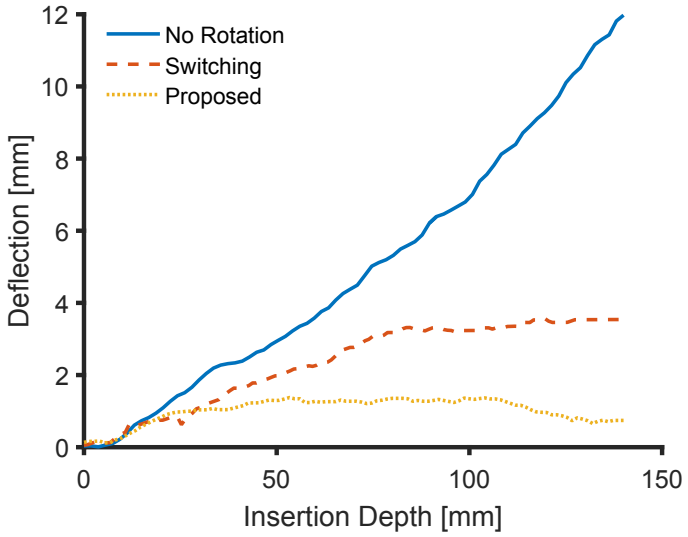

Figure 5.5: Comparison of the resultant needle tip deflection results for the No Rotation, Switching, and Proposed Method trials. The needle was initialized with a bevel position of 0°.

each of the eight different bevel angle starting conditions. The "Proposed Method" trials are performed twice at each of the eight different bevel angle starting conditions, for a total of sixteen trials implemented using our 3D needle steering controller. A comparison of the overall deflection results for the "No Rotation", "Switching" and one of the "Proposed Method" trials using an initial bevel position of 0° is shown in Fig. 5.5. The x, y, and resultant deflection results for each of these cases is shown in Table 5.1. A visual representation of the data is shown in Fig. 5.6 in the form of a box plot graph.

A paired sample t-test was performed, comparing the "Switching" and "Proposed Method" results to those from the "No Rotation" trials. As well, a second paired sample t-test was performed comparing the "Proposed Method" results to those from the "Switching" trials. The results are summarized in Table 5.2.

An example of one of the Switching trials is shown in Fig. 5.7. In this example, the needle's bevel position was initialized to 45°. In comparison, an example of one of the Proposed Method trials is shown in Fig. 5.8, where the needle's x and y deflections as well as the needle's bevel position is plotted

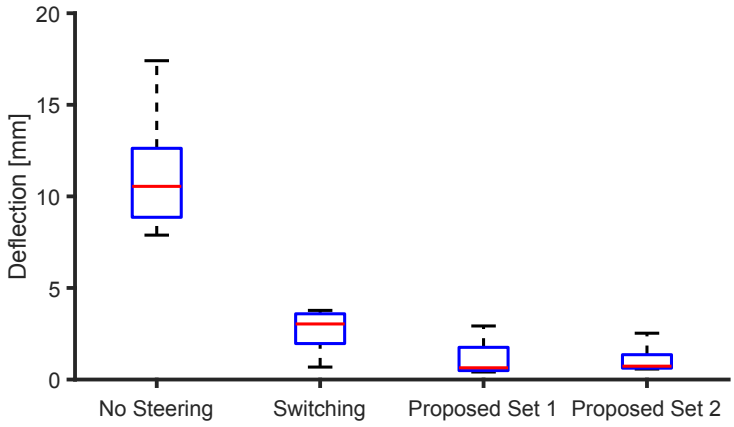

Figure 5.6: Boxplot comparisons of the No Steering, Switching, and Proposed steering methods.

Table 5.2: Summary of Paired Sample t-Test Statistics

	No Rotation	**Switching**	**Proposed Method Set 1**	**Proposed Method Set 2**
Abs. Mean Deflection [mm]	11.2	2.7	1.1	1.1
Standard Deviation [mm]	3.1	1.1	0.9	0.7
t Statistic (Relative to No Rotation)	-	6.7	8.9	8.5
p Value (Relative to No Rotation)	-	2.8×10^{-4}	4.8×10^{-5}	6.3×10^{-5}
t Statistic (Relative to Switching)	-	-	2.5	4.3
p Value (Relative to Switching)	-	-	2.7×10^{-2}	3.7×10^{-3}

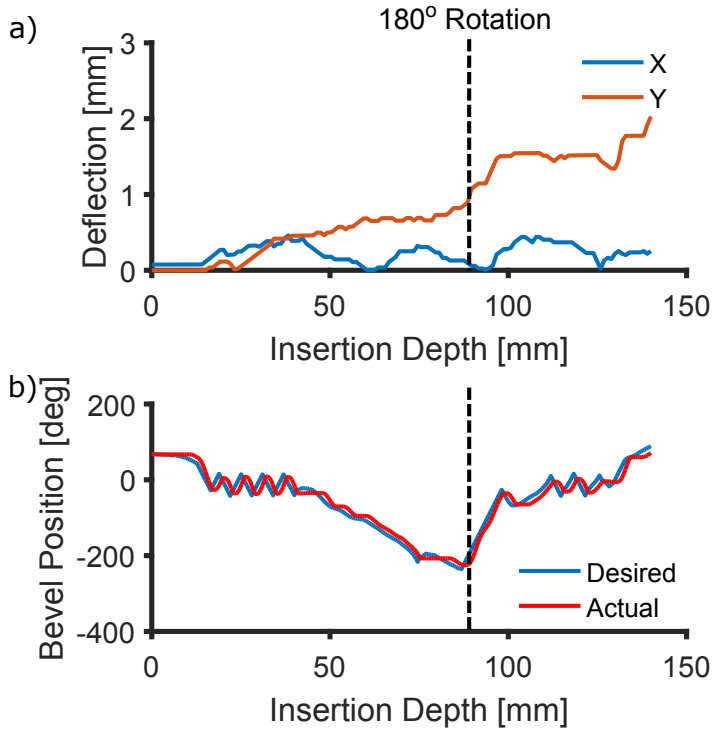

Figure 5.7: Example of one of the Switching trials that combine VDC with 180° rotations. In a), the needle's deflection versus insertion depth is shown while in b), the needle's bevel angle versus insertion depth is shown. In this example, the bevel angle was initialized at 45°.

against the insertion depth. In this example, the needle's bevel position was also initialized to 45°.

5.5 Discussion

As shown in Table 5.1, with no rotation, at the maximum depth of 140 mm the absolute mean x-axis deflection came to 7.3 mm, the absolute mean y-axis deflection came to 7.1 mm, and the resultant mean needle deflection came to 11.2 mm.

Results showed that without needle steering, the needle would deflect with an average deflection of 11.2 mm. Using the switching approach, the overall needle deflection was reduced to 2.7 mm, and using the proposed 3D needle

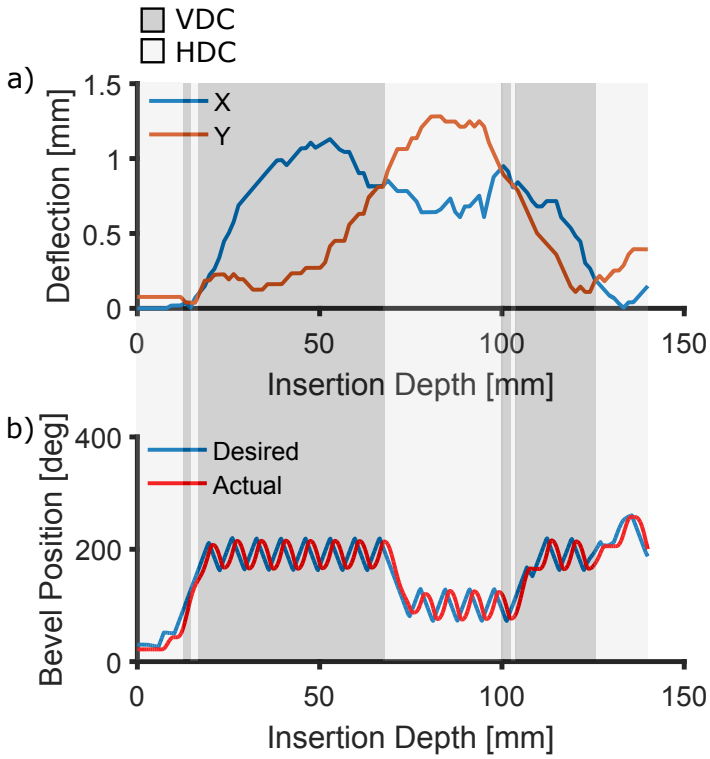

Figure 5.8: Example of one of the Proposed Method steering trials. In a), the needle's deflection versus the depth is shown while in b), the needle's bevel angle versus the depth is shown. In this example, the bevel angle was initialized at 45°.

steering approach, the overall needle deflection was reduced to an average of 1.1 mm. A paired-sample t-test was used to compare the needle deflection results under the switching method and under the proposed 3D needle steering method. Results showed a significant reduction in overall deflection using the 3D needle steering approach at the 5% significance level.

Through the implementation of our VDC with switching approach, there was a significant decrease in both the x-axis and y-axis deflection. The most significant reduction in deflection occurred along the x-axis, which was controlled using our VDC controller. The x deflection changed from 7.3 mm with no rotation to 0.4 mm using the switching approach. This demonstrates that the VDC controller can achieve sub-millimeter deflection minimization with respect to the x-axis. However, while the y-axis deflection did decrease with respect to the no rotation set of trials, from a mean of 7.1 mm with no rotation to a mean of 2.7 mm with the switching controller, the deflection was still significantly greater than that along the x-axis. This is to be expected, since the y-axis deflection was only controlled using a simple threshold-based algorithm which caused the needle to rotate 180° once the y-axis deflection became greater than 1 mm. While this is not optimal, it is a simple, easily implemented design that can achieve consistent results on-par with typical manual PPB insertions.

Our 3D steering method that implemented both VDC and HDC resulted in the greatest reduction in needle deflection. In the first set of trials (Proposed Method Set 1), the mean x-axis deflection was 0.5 mm and the mean y-axis deflection was 1.0 mm, with a resultant mean deflection of 1.1 mm. In the second set of trials (Proposed Method Set 2), the mean x-axis deflection was 0.9 mm and the mean y-axis deflection was 0.5 mm, with a resultant mean deflection of 1.1 mm. This is a significant improvement over both the no rotation and switching cases, and demonstrates the capabilities of our proposed 3D needle steering approach. Again, this is to be expected, since our 3D needle steering approach shifts between two controllers, both designed to actively reduce de-

flection along their respective axes, whereas the switching approach uses one controller to handle deflection along the x-axis combined with 180° degree rotations to reduce deflection along the y-axis. While the switching method offers a simple way to help steer the needle, our proposed 3D steering approach offers a much more robust, controlled approach for deflection minimization, since focus can quickly be diverted from one axis to the other when appropriate, i.e. whenever the deflection along one axis exceeds that of the other.

The paired sample t-test results shown in Table 5.2 support the claim that there is a statistically significant reduction in deflection using the Switching and 3D Steering control methods at the 5% significance level, as shown by the t statistics and p values labeled as "Relative to No Rotation" in Table 5.2. Furthermore, the table also shows that there is a statistically significant reduction in deflection from the Switching approach using our proposed 3D steering method, as shown by the t statistics and p values labeled as "Relative to Switching" in Table 5.2.

Through the use of our proposed method, and by limiting our rotational velocity to a maximum of 180°/s, we reduce the need to "drill" the needle into tissue. While drilling motions can be used to reduce the impact of asymmetrical bevel-tipped needles, these type of steering motions have the potential to transmit large amounts of energy and friction-induced heat to the tissue. This could have consequences in terms of tissue trauma, swelling, and recovery. Our proposed method does not require periods of constant, high-velocity needle rotation, opting instead for more controlled, calculated, and necessary steering motions performed over the course of the entire needle insertion process. We also feel that surgeons would feel more comfortable with a system like the one proposed in this chapter, which incorporate more controlled steering motions than ones that use periods of higher velocity, continual rotation such as duty-cycling approaches. As well, the majority of duty-cycling controllers have only been tested using extremely flexible, nitinol wire with a radius of less than

0.7 mm, which can achieve curvatures that may be impossible to obtain using clinical, higher-gauge needles.

There were some inconsistencies in the needle insertion trials, with 3 of the 16 trials reaching deflections of greater than 2 mm. This is most likely attributed to tissue heterogeneity combined with tracks left from previous needle insertions subtly affecting the needle's insertion trajectory. However, these deflection results are still an improvement over manual steering capabilities. As well, in manual steering, surgeons may or may not achieve an optimal insertion on the first try; some insertions could require 3 or more tries before achieving a satisfactory result. The method proposed in this chapter is capable of achieving consistent results better than manual insertion methods. As well, the vast majority of the needle insertion trials performed in Section 3.5 resulted in sub-millimeter needle deflections, which are very difficult to achieve consistently during manual needle insertion procedures, even for experienced surgeons.

The needle steering method proposed here is intended to enhance the needle steering capabilities of physicians performing percutaneous needle insertion procedures. By incorporating a needle rotation controller into these type of medical procedures, we can assist surgeons by increasing their accuracy and consistency during the needle insertion process. This could greatly benefit new surgeons, who do not yet have the experience and skill required to achieve consistent needle insertions compared to more experienced surgeons. By sharing some of the work-load with a robotic assistant, we can decrease the length of training necessary for surgeons to become competent at procedures such as PPB. As well, by increasing the number of surgeons who are able to perform these surgeries, we can increase patient access to the procedure and reduce wait times. This is extremely relevant for diseases like cancer, where time can be a factor due to the fact that the disease can spread to other parts of the body if left unchecked for too long.

5.6 Concluding Remarks

In this chapter, we describe a method for controlling needle deflection through the use of multiple 2D planar controllers, each designed using an integrator-backstepping control approach. One controller implements Vertical Deflection Control to reduce needle deflection outside of the $y-z$ plane while the second controller implements Horiontal Deflection Control to reduce deflection outside of the $x-z$ plane. By properly shifting between the two controllers, we attempt to minimize the overall needle deflection.

Our needle insertion setup consisted of a two degree-of-freedom surgical robot designed to insert the needle at a constant velocity while adjusting the needle's rotational velocity to allow for needle steering via our derived controllers. Needle insertions were performed using an 18 gauge bevel-tipped brachytherapy needle and a dual-layered heterogeneous tissue phantom composed of 100 mm of *ex-vivo* pork tissue followed by a 70 mm layer of *ex-vivo* beef tissue.

Needle insertion experiments were performed in order to compare the use of our proposed 3D needle steering method to trials without using any type of needle steering algorithm, as well as to trials involving the use of our VDC controller combined with a threshold-based 180° switching algorithm. Compared to an average needle tip deflection of 11.2 mm at a depth of 140 mm without rotation, and an average of 2.7 mm using the switching approach, our 3D needle steering approach was able to significantly reduce needle deflection to an average of less than 1.1 mm.

Chapter 6

Conclusion

In Chapter 3, a method for visualizing 3D needle shapes using 2D transverse US images is described. *In-vitro* experiments using a plastisol tissue phantom are performed in order to identify how many and at what depth transverse images should be captured in order to obtain accurate needle shape estimates. Results showed that in order to obtain maximum errors of less than 2 mm, the depth of the final image within the transverse image set must be at least 75% of the maximum needle depth into tissue. Using 10 transverse images closest to the needle tip, the proposed method is functional as long as the needle can be identified in 30% of the images obtained. The proposed method was also applied to *in-vivo* US images obtained from PPB procedures and was validated using images obtained from the sagittal perspective. Results showed a maximum error averaging 0.70 mm when using the entire transverse image sets and 0.91 mm when using the 5 transverse image sets.

In Chapter 4 we introduce a method for automatic needle tracking using 2D transverse US images by combining our image processing method described in Chapter 4 with a Kalman filtering algorithm. Our needle tracking method is then demonstrated using a semi-automatic needle steering system and an *ex-vivo* beef tissue phantom. The needle deflection results obtained from the tracking algorithm are used to fully parameterize a needle-tissue interaction

model, which allows us to predict the needle's future tip deflection. The semi-automatic needle steering process demonstrated in this chapter is divided into two phases. In the first phase, the US probe constantly tracks the needle tip, allowing us to gather data of the needle's tip deflection to inform our needle-tissue interaction model. In the second phase, the US probe is stopped midway while the needle continues to be inserted. The needle-tissue interaction model is used to predict the needle's future tip deflection without the need for actual imaging feedback. This allows us to reduce the application of unnecessary forces and reduce the amount of tissue deformation caused by the US probe near the target area. Results showed that, without rotation, the deflection of the needle tip can be predicted with an average accuracy of 1.0 mm, ranging from 0.1 mm to 2.6 mm. With one rotation, the deflection of the needle tip can be predicted with an average accuracy of 0.7 mm, ranging from 0.1 mm to 2.4 mm.

In Chapter 5 we present a method for 3D needle steering using a combination of 2D planar controllers. Each controller is designed using an integrator-backstepping control approach. One controller implements Vertical Deflection Control (VDC), used to minimize deflection of the needle's tip away from the vertical plane. The second controller implements Horizontal Deflection Control (HDC), used to minimize the needle's tip deflection away from the horizontal plane. We shift between these two controllers based on which plane contains the greatest error, allowing us to reduce the total needle deflection. The performance of our proposed needle steering approach is demonstrated through the use of a multi-layered *ex-vivo* pork and beef tissue phantom. We compare the results to a controller that implements VDC combined with 180° rotations. Results showed that without any type of needle steering, the average needle tip deflection was 11.2 mm at the maximum depth of 140 mm. Using the switching method, the average needle tip deflection was 2.7 mm at the maximum depth, and our 3D needle steering approach reduced the needle tip deflection to an

average of 1.1 mm at the maximum depth. The proposed method is intended to help enhance the abilities of PPB surgeons through the use of a robotic needle steering assistant designed to aid with needle steering during the insertion process.

6.1 Future Work

Some of the ways that the work proposed in this thesis can be expanded upon in the future include:

1. In Chapter 4, further work can be performed in automating the process of obtaining the transverse US image set used to parameterize the needle's 3D shape. By programming a surgical robot to adjust the US probe manually to obtain the transverse images, the surgeon can divert their focus to more important issues, such as preparing the next brachytherapy needle, while the needle's shape is automatically generated.

2. In Chapter 5, the needle-tissue interaction model only incorporates single 180° rotations of the needle. Further work can be performed in developing a more robust model that can predict the needle's tip deflection when multiple rotations are used.

3. The beef/pork tissue phantoms used in Chapters 5 and 6 of this thesis were useful in simulating biological tissue, but in the future, the development of tissue phantoms that better simulate the way in which the prostate gland is embedded within surrounding tissue could be explored.

4. In Chapter 6, we used basic methods to estimate α, β, and γ. Additional work can be performed on incorporating more accurate ways to estimate α, β, and γ, possibly through the use of state observers.

5. In Chapter 6, we assumed that the radius of curvature κ was a constant value. We could develop a more robust control method by using methods to parameterize κ during the insertion process.

6. In Chapter 6, we discussed ways to reduce tissue trauma by limiting the velocity and frequency of needle rotation during the steering process. There has been relatively little research on precisely how needle drilling affects biological tissue. Future work could involve exploring this topic in further detail.

Bibliography

[1] Canadian Cancer Society's Advisory Committee on Cancer Statistics. *Canadian Cancer Statistics*. Canadian Cancer Society, Toronto, ON, May 2014.

[2] Komanduri KN Charyulu. Transperineal interstitial implantation of prostate cancer: a new method. *International Journal of Radiation Oncology* Biology* Physics*, 6(9):1261–1266, 1980.

[3] Al V Taira, Gregory S Merrick, Robert W Galbreath, Kent E Wallner, and Wayne M Butler. Natural history of clinically staged low-and intermediate-risk prostate cancer treated with monotherapeutic permanent interstitial brachytherapy. *International Journal of Radiation Oncology* Biology* Physics*, 76(2):349–354, 2010.

[4] Brian J Davis, Eric M Horwitz, W Robert Lee, Juanita M Crook, Richard G Stock, Gregory S Merrick, Wayne M Butler, Peter D Grimm, Nelson N Stone, Louis Potters, et al. American Brachytherapy Society consensus guidelines for transrectal ultrasound-guided permanent prostate brachytherapy. *Brachytherapy*, 11(1):6–19, 2012.

[5] GA Chapman, D Johnson, and AR Bodenham. Visualisation of needle position using ultrasonography. *Anaesthesia*, 61(2):148–158, 2006.

[6] Paul M Novotny, Jeff A Stoll, Nikolay V Vasilyev, Pedro J Del Nido, Pierre E Dupont, Todd E Zickler, and Robert D Howe. GPU based real-

time instrument tracking with three-dimensional ultrasound. *Medical image analysis*, 11(5):458–464, 2007.

[7] Hua Zhou, Wu Qiu, Mingyue Ding, and Songgen Zhang. Automatic needle segmentation in 3D ultrasound images using 3D improved Hough transform. In *Medical Imaging*, pages 691821–691821. International Society for Optics and Photonics, 2008.

[8] Wu Qiu, Ming Yuchi, Mingyue Ding, David Tessier, and Aaron Fenster. Needle segmentation using 3D Hough transform in 3D TRUS guided prostate transperineal therapy. *Medical physics*, 40(4):042902, 2013.

[9] Mingyue Ding, Zhouping Wei, Lori Gardi, Donal B Downey, and Aaron Fenster. Needle and seed segmentation in intra-operative 3D ultrasound-guided prostate brachytherapy. *Ultrasonics*, 44:e331–e336, 2006.

[10] Wu Qiu, Ming Yuchi, and Mingyue Ding. Phase grouping-based needle segmentation in 3-d trans-rectal ultrasound-guided prostate trans-perineal therapy. *Ultrasound in medicine & biology*, 40(4):804–816, 2014.

[11] Hamid Reza Sadeghi Neshat and Rajni V Patel. Real-time parametric curved needle segmentation in 3D ultrasound images. In *Biomedical Robotics and Biomechatronics, 2008. BioRob 2008. 2nd IEEE RAS & EMBS International Conference on*, pages 670–675. IEEE, 2008.

[12] Mohammad Aboofazeli, Purang Abolmaesumi, Parvin Mousavi, and Gabor Fichtinger. A new scheme for curved needle segmentation in three-dimensional ultrasound images. In *Biomedical Imaging: From Nano to Macro, 2009. ISBI'09. IEEE International Symposium on*, pages 1067–1070. IEEE, 2009.

[13] Zhouping Wei, Lori Gardi, Dónal B Downey, and Aaron Fenster. Oblique needle segmentation for 3D TRUS-guided robot-aided transper-

ineal prostate brachytherapy. In *Biomedical Imaging: Nano to Macro, 2004. IEEE International Symposium on*, pages 960–963. IEEE, 2004.

[14] Mingyue Ding and Aaron Fenster. A real-time biopsy needle segmentation technique using Hough transform. *Medical physics*, 30(8):2222–2233, 2003.

[15] Marian Uhercik, Jan Kybic, Hervé Liebgott, and Christian Cachard. Model fitting using RANSAC for surgical tool localization in 3-d ultrasound images. *Biomedical Engineering, IEEE Transactions on*, 57(8): 1907–1916, 2010.

[16] Martin Barva, Jan Kybic, Jean-Martial Mari, Christian Cachard, and Václav Hlavác. Automatic localization of curvilinear object in 3D ultrasound images. In *Medical Imaging*, pages 455–462. International Society for Optics and Photonics, 2005.

[17] Yue Zhao, Hervé Liebgott, and Christian Cachard. Tracking biopsy needle using Kalman filter and RANSAC algorithm with 3D ultrasound. *Acoustics 2012 Nantes*, 2012.

[18] Ki Jinn Chin, Anahi Perlas, Vincent WS Chan, and Richard Brull. Needle visualization in ultrasound-guided regional anesthesia: challenges and solutions. *Regional anesthesia and pain medicine*, 33(6):532–544, 2008.

[19] Mert Kaya and Ozkan Bebek. Needle localization using gabor filtering in 2D ultrasound images. In *Robotics and Automation (ICRA), 2014 IEEE International Conference on*, pages 4881–4886. IEEE, 2014.

[20] Mert Kaya and Ozkan Bebek. Gabor filter based localization of needles in ultrasound guided robotic interventions. In *Imaging Systems and Techniques (IST), 2014 IEEE International Conference on*, pages 112–117, Oct 2014. doi: 10.1109/IST.2014.6958456.

[21] Stephen H Okazawa, Richelle Ebrahimi, Jason Chuang, Robert N Rohling, and Septimiu E Salcudean. Methods for segmenting curved needles in ultrasound images. *Medical image analysis*, 10(3):330–342, 2006.

[22] Alper Ayvaci, Pingkun Yan, Sheng Xu, Stefano Soatto, and Jochen Kruecker. Biopsy needle detection in transrectal ultrasound. *Computerized Medical Imaging and Graphics*, 35(7):653–659, 2011.

[23] Kim Mathiassen, Diego Dall'Alba, Riccardo Muradore, Paolo Fiorini, and Ole Jakob Elle. Real-time biopsy needle tip estimation in 2D ultrasound images. In *Robotics and Automation (ICRA), 2013 IEEE International Conference on*, pages 4363–4369. IEEE, 2013.

[24] Zipi Neubach and Moshe Shoham. Ultrasound-guided robot for flexible needle steering. *Biomedical Engineering, IEEE Transactions on*, 57(4): 799–805, 2010.

[25] Jay Carriere, Carlos Rossa, Ron Sloboda, Nawaid Usmani, and Mahdi Tavakoli. Needle shape estimation in soft tissue based on partial ultrasound image observation. In *Robotics & Automation (ICRA), 2015 IEEE International Conf. on*, May 2015.

[26] Joseph D Greer, Troy K Adebar, Gloria L Hwang, and Allison M Okamura. Real-time 3D curved needle segmentation using combined b-mode and power doppler ultrasound. In *Medical Image Computing and Computer-Assisted Intervention–MICCAI 2014*, pages 381–388. Springer, 2014.

[27] Troy K Adebar, Ashley E Fletcher, and Allison M Okamura. 3-D ultrasound-guided robotic needle steering in biological tissue. *Biomedical Engineering, IEEE Transactions on*, 61(12):2899–2910, 2014.

[28] Gustaaf J Vrooijink, Momen Abayazid, and Sarthak Misra. Real-time three-dimensional flexible needle tracking using two-dimensional ultra-

sound. In *Robotics and Automation (ICRA), 2013 IEEE International Conference on*, pages 1688–1693. IEEE, 2013.

[29] Gustaaf J Vrooijink, Momen Abayazid, Sachin Patil, Ron Alterovitz, and Sarthak Misra. Needle path planning and steering in a three-dimensional non-static environment using two-dimensional ultrasound images. *The International Journal of Robotics Research*, page 0278364914526627, 2014.

[30] Ping Yan, John C Cheeseborough, and KS Clifford Chao. Automatic shape-based level set segmentation for needle tracking in 3-d TRUS-guided prostate brachytherapy. *Ultrasound in medicine & biology*, 38(9):1626–1636, 2012.

[31] Niki Abolhassani, Rajni Patel, and Mehrdad Moallem. Needle insertion into soft tissue: A survey. *Medical engineering & physics*, 29(4):413–431, 2007.

[32] Niki Abolhassani and RajniV Patel. Deflection of a flexible needle during insertion into soft tissue. In *Engineering in Medicine and Biology Society, 2006. EMBS'06. 28th Annual International Conference of the IEEE*, pages 3858–3861. IEEE, 2006.

[33] R.J. Roesthuis, Youri R.J. van Veen, A. Jahya, and S. Misra. Mechanics of needle-tissue interaction. In *Intelligent Robots and Systems (IROS), 2011 IEEE/RSJ International Conference on*, pages 2557–2563, Sept 2011. doi: 10.1109/IROS.2011.6094969.

[34] Momen Abayazid, Roy J Roesthuis, Rob Reilink, and Sarthak Misra. Integrating deflection models and image feedback for real-time flexible needle steering. *Robotics, IEEE Transactions on*, 29(2):542–553, 2013.

[35] Simon P DiMaio and Septimiu E Salcudean. Needle insertion modeling

and simulation. *Robotics and Automation, IEEE Transactions on*, 19(5): 864–875, 2003.

[36] Simon P DiMaio and SE Salcudean. Needle steering and motion planning in soft tissues. *Biomedical Engineering, IEEE Transactions on*, 52(6): 965–974, 2005.

[37] Vinutha Kallem and Noah J Cowan. Image guidance of flexible tip-steerable needles. *Robotics, IEEE Transactions on*, 25(1):191–196, 2009.

[38] John P Swensen and Noah J Cowan. Torsional dynamics compensation enhances robotic control of tip-steerable needles. In *Robotics and Automation (ICRA), 2012 IEEE International Conference on*, pages 1601–1606. IEEE, 2012.

[39] B. Fallahi, C. Rossa, R. S. Sloboda, N. Usmani, and M. Tavakoli. Sliding-based switching control for image-guided needle steering in soft tissue. *IEEE Robotics and Automation Letters*, 1(2):860–867, July 2016. ISSN 2377-3766. doi: 10.1109/LRA.2016.2528293.

[40] Mohsen Khadem, Carlos Rossa, Ron S. Sloboda, Nawaid Usmani, and Mahdi Tavakoli. Ultrasound-guided model predictive control of needle steering in biological tissue. *Journal of Medical Robotics Research*, 01(01): 1640007, 2016. doi: 10.1142/S2424905X16400079. URL http://www.worldscientific.com/doi/abs/10.1142/S2424905X16400079.

[41] Daniel Glozman and Moshe Shoham. Image-guided robotic flexible needle steering. *Robotics, IEEE Transactions on*, 23(3):459–467, 2007.

[42] Septimiu E Salcudean, Thomas D Prananta, William J Morris, and Ingrid Spadinger. A robotic needle guide for prostate brachytherapy. In *Robotics and Automation, 2008. ICRA 2008. IEEE International Conference on*, pages 2975–2981. IEEE, 2008.

[43] Gabor Fichtinger, Jonathan P Fiene, Christopher W Kennedy, Gernot Kronreif, Iulian Iordachita, Danny Y Song, Everette C Burdette, and Peter Kazanzides. Robotic assistance for ultrasound-guided prostate brachytherapy. *Medical image analysis*, 12(5):535–545, 2008.

[44] Danny Y Song, Everette C Burdette, Jonathan Fiene, Elwood Armour, Gernot Kronreif, Anton Deguet, Zhe Zhang, Iulian Iordachita, Gabor Fichtinger, and Peter Kazanzides. Robotic needle guide for prostate brachytherapy: clinical testing of feasibility and performance. *Brachytherapy*, 10(1):57–63, 2011.

[45] Jur Van Den Berg, Sachin Patil, Ron Alterovitz, Pieter Abbeel, and Ken Goldberg. LQG-based planning, sensing, and control of steerable needles. In *Algorithmic Foundations of Robotics IX*, pages 373–389. Springer, 2011.

[46] Kyle B Reed, Vinutha Kallem, Ron Alterovitz, Ken Goldbergxz, Allison M Okamura, and Noah J Cowan. Integrated planning and image-guided control for planar needle steering. In *Biomedical Robotics and Biomechatronics, 2008. BioRob 2008. 2nd IEEE RAS & EMBS International Conference on*, pages 819–824. IEEE, 2008.

[47] Thomas R Wedlick and Allison M Okamura. Characterization of precurved needles for steering in tissue. In *Engineering in Medicine and Biology Society, 2009. EMBC 2009. Annual International Conference of the IEEE*, pages 1200–1203. IEEE, 2009.

[48] B Todd Sitzman and David R Uncles. The effects of needle type, gauge, and tip bend on spinal needle deflection. *Anesthesia & Analgesia*, 82(2): 297–301, 1996.

[49] Pierre E Dupont, Jesse Lock, Brandon Itkowitz, and Evan Butler. Design and control of concentric-tube robots. *Robotics, IEEE Transactions on*, 26(2):209–225, 2010.

[50] D Caleb Rucker, Robert J Webster, Gregory S Chirikjian, and Noah J Cowan. Equilibrium conformations of concentric-tube continuum robots. *The International journal of robotics research*, 2010.

[51] Robert J Webster and Bryan A Jones. Design and kinematic modeling of constant curvature continuum robots: A review. *The International Journal of Robotics Research*, 2010.

[52] Seong Young Ko, Luca Frasson, et al. Closed-loop planar motion control of a steerable probe with a programmable bevel inspired by nature. *Robotics, IEEE Transactions on*, 27(5):970–983, 2011.

[53] D Caleb Rucker, Joydeep Das, Hunter B Gilbert, Philip J Swaney, Michael I Miga, Niladri Sarkar, and Robert J Webster. Sliding mode control of steerable needles. *Robotics, IEEE Transactions on*, 29(5):1289–1299, 2013.

[54] Davneet S Minhas, Johnathan A Engh, Michele M Fenske, and Cameron N Riviere. Modeling of needle steering via duty-cycled spinning. In *Engineering in Medicine and Biology Society, 2007. EMBS 2007. 29th Annual International Conference of the IEEE*, pages 2756–2759. IEEE, 2007.

[55] Kaiguo Yan, Wan Sing Ng, Keck Voon Ling, Tien-I Liu, Yan Yu, and Tarun Podder. High frequency translational oscillation & rotational drilling of the needle in reducing target movement. In *Computational Intelligence in Robotics and Automation, 2005. CIRA 2005. Proceedings. 2005 IEEE International Symposium on*, pages 163–168. IEEE, 2005.

[56] Peter Marhofer and Vincent WS Chan. Ultrasound-guided regional anesthesia: current concepts and future trends. *Anesthesia & Analgesia*, 104 (5):1265–1269, 2007.

[57] AV D'Amico, CM Tempany, R Cormack, N Hata, M Jinzaki, K Tuncali,

M Weinstein, and JP Richie. Transperineal magnetic resonance image guided prostate biopsy. *The Journal of urology*, 164(2):385–387, 2000.

[58] J Hong, Takeyoshi Dohi, Makoto Hashizume, K Konishi, and N Hata. An ultrasound-driven needle-insertion robot for percutaneous cholecystostomy. *Physics in Medicine and Biology*, 49(3):441, 2004.

[59] Louis Potters, Carol Morgenstern, Emil Calugaru, Paul Fearn, Anup Jassal, Joseph Presser, and Edward Mullen. 12-year outcomes following permanent prostate brachytherapy in patients with clinically localized prostate cancer. *The Journal of urology*, 173(5):1562–1566, 2005.

[60] Xu Wen, S.E. Salcudean, and P.D. Lawrence. Detection of brachytherapy seeds using 3-d transrectal ultrasound. *Biomedical Engineering, IEEE Transactions on*, 57(10):2467–2477, Oct 2010. ISSN 0018-9294.

[61] Rafael C. Gonzalez, Richard E. Woods, and Steven L. Eddins. *Digital Image Processing Using MATLAB*. Prentice Hall Press, Upper Saddle River, NJ, USA, 2007. ISBN 1405893281, 9781405893282.

[62] Yongjian Yu and Scott T Acton. Speckle reducing anisotropic diffusion. *Image Processing, IEEE Transactions on*, 11(11):1260–1270, 2002.

[63] Santiago Aja-Fernández and Carlos Alberola-López. On the estimation of the coefficient of variation for anisotropic diffusion speckle filtering. *Image Processing, IEEE Transactions on*, 15(9):2694–2701, 2006.

[64] Ron Alterovitz, Ken Goldberg, and Allison Okamura. Planning for steerable bevel-tip needle insertion through 2D soft tissue with obstacles. In *Robotics and Automation, 2005. ICRA 2005. Proceedings of the 2005 IEEE International Conference on*, pages 1640–1645. IEEE, 2005.

[65] Kyle B Reed, Ann Majewicz, Vinutha Kallem, Ron Alterovitz, Ken Goldberg, Noah J Cowan, and Allison M Okamura. Robot-assisted needle steering. *Robotics & Automation Magazine, IEEE*, 18(4):35–46, 2011.

[66] Martin A Fischler and Robert C Bolles. Random sample consensus: a paradigm for model fitting with applications to image analysis and automated cartography. *Communications of the ACM*, 24(6):381–395, 1981.

[67] M. Zuliani. RANSAC toolbox for MATLAB. [web page] http://www.mathworks.com/matlabcentral/fileexchange/18555, Nov. 2008. [Accessed on: August 1, 2014].

[68] Philip HS Torr and Andrew Zisserman. MLESAC: A new robust estimator with application to estimating image geometry. *Computer Vision and Image Understanding*, 78(1):138–156, 2000.

[69] Gang Wan, Zhouping Wei, Lori Gardi, Donal B Downey, and Aaron Fenster. Brachytherapy needle deflection evaluation and correction. *Medical Physics*, 32(4):902–909, 2005.

[70] Yue Zhao, Hervé Liebgott, and Christian Cachard. Tracking micro tool in a dynamic 3D ultrasound situation using kalman filter and ransac algorithm. In *Biomedical Imaging (ISBI), 2012 9th IEEE International Symposium on*, pages 1076–1079. IEEE, 2012.

[71] Y Zhao, H Liebgott, and C Cachard. Tracking biopsy needle using Kalman filter and RANSAC algorithm with 3D ultrasound. In *Proceedings of the Acoustics 2012 Nantes Conference*, pages 231–236, 2012.

[72] Pierre Chatelain, Alexandre Krupa, and Maud Marchal. Real-time needle detection and tracking using a visually servoed 3D ultrasound probe. In *Robotics and Automation (ICRA), 2013 IEEE International Conference on*, pages 1676–1681. IEEE, 2013.

[73] Thomas Lehmann, Carlos Rossa, Nawaid Usmani, Ronald Sloboda, and Mahdi Tavakoli. A virtual sensor for needle deflection estimation during soft-tissue needle insertion. In *Robotics and Automation (ICRA), 2015 IEEE International Conference on*, pages 1217–1222. IEEE, 2015.

[74] Thomas Lehmann, Mahdi Tavakoli, Nawaid Usmani, and Ronald Sloboda. Force-sensor-based estimation of needle tip deflection in brachytherapy. *Journal of Sensors*, 2013, 2013.

[75] Richard Taschereau, Jean Pouliot, Jean Roy, and Daniel Tremblay. Seed misplacement and stabilizing needles in transperineal permanent prostate implants. *Radiotherapy and Oncology*, 55(1):59–63, 2000.

[76] Noah J Cowan, Ken Goldberg, Gregory S Chirikjian, Gabor Fichtinger, Ron Alterovitz, Kyle B Reed, Vinutha Kallem, Wooram Park, Sarthak Misra, and Allison M Okamura. Robotic needle steering: Design, modeling, planning, and image guidance. In *Surgical Robotics*, pages 557–582. Springer, 2011.

[77] Allison M Okamura, Christina Simone, and Mark Leary. Force modeling for needle insertion into soft tissue. *Biomedical Engineering, IEEE Transactions on*, 51(10):1707–1716, 2004.

[78] M. Khadem, C. Rossa, R. S. Sloboda, N. Usmani, and M. Tavakoli. Mechanics of tissue cutting during needle insertion in biological tissue. *IEEE Robotics and Automation Letters*, 1(2):800–807, July 2016. ISSN 2377-3766. doi: 10.1109/LRA.2016.2528301.

[79] C. Rossa, M. Khadem, R. Sloboda, N. Usmani, and M. Tavakoli. Adaptive quasi-static modelling of needle deflection during steering in soft tissue. *IEEE Robotics and Automation Letters*, 1(2):916–923, July 2016. ISSN 2377-3766. doi: 10.1109/LRA.2016.2527065.

[80] Robert J Webster, Jin Seob Kim, Noah J Cowan, Gregory S Chirikjian, and Allison M Okamura. Nonholonomic modeling of needle steering. *The International Journal of Robotics Research*, 25(5-6):509–525, 2006.

[81] Hassan K Khalil and JW Grizzle. *Nonlinear systems*, volume 3. Prentice hall New Jersey, 1996.